An Examination of Local versus Nonlocal Aspects of a TKE-Based Boundary Layer Scheme in Clear Convective Conditions

STÉPHANE BÉLAIR AND JOCELYN MAILHOT

Recherche en Prévision Numérique, Atmospheric Environment Service, Dorval, Quebec, Canada

J. WALTER STRAPP

Cloud Physics Research Division, Atmospheric Environment Service, Downsview, Ontario, Canada

J. IAN MACPHERSON

Institute for Aerospace Research, National Research Council, Ottawa, Ontario, Canada

(Manuscript received 15 June 1998, in final form 3 October 1998)

ABSTRACT

In this study, the ability of a turbulent kinetic energy (TKE)–based boundary layer scheme to reproduce the rapid evolution of the planetary boundary layer (PBL) observed during two clear convective days is examined together with the impact of including nonlocal features in the boundary layer scheme. The two cases are chosen from the Montreal-96 Experiment on Regional Mixing and Ozone (MERMOZ): one is characterized by strong buoyancy, a strong capping inversion, and weak vertical wind shear; the other displays moderate buoyancy, a weaker subsidence inversion, and significant wind shear near the PBL top. With the original local version of the turbulence scheme, the model reproduces the vertical structures and turbulent quantities observed in the well-developed boundary layer for the first case. For the second case, the model fails to reproduce the rapid evolution of the boundary layer even though the TKE and sensible heat fluxes are greatly overpredicted.

Some nonlocal aspects of the turbulence scheme are tested for these two cases. Inclusion of nonlocal (countergradient) terms in the vertical diffusivity equation has little impact on the simulated PBL. In contrast, alternative formulations of the turbulent length scales that follow the strategy proposed by Bougeault and Lacarrère have a greater influence. With the new turbulent lengths, entrainment at the top of the boundary layer is enhanced so that the depth of the well-mixed layer is much larger compared to that of the local simulations even though the turbulent sensible heat fluxes are smaller. Comparison with observations reveals, however, that the inclusion of these modifications does not improve all aspects of the simulation. To improve the performance and reduce somewhat the arbitrariness in the Bougeault–Lacarrère technique, a relationship between the two turbulent length scales (mixing and dissipation) used in the turbulence scheme is proposed. It is shown that, in addition to reducing the sensitivity of the results to the particular formulations, the simulated boundary layer agrees better with observations.

1. Introduction

It is important for mesoscale and large-scale atmospheric models to represent adequately the characteristics (temperature, humidity, turbulence) and evolution of the planetary boundary layer (PBL), not only because it is the part of the atmosphere in which human activity is concentrated, but also because this layer plays a major role in weather and air quality simulations. For example, the onset and intensity of convective cloud activity depend on the characteristics of the PBL, since moist convection (deep or shallow) has its roots in the PBL. A large variety of physical schemes for representing the turbulent PBL have been developed by atmospheric modelers in the past decades (see Holt and Raman 1988; Stull 1988; Garratt et al. 1996). A wide range of strategies, both local and nonlocal types, have been applied with varying degrees of success.

For the local type of closures, the turbulent fluxes of momentum, heat, and humidity at one point are determined from mean atmospheric variables and/or their gradients at that point using turbulence closures of the first order (e.g., O'Brien 1970; Pielke and Mahrer 1975), order 1.5 (e.g., Mailhot and Benoit 1982; Mellor and Yamada 1982; Therry and Lacarrère 1983), second order (e.g., Mellor and Yamada 1974; Abdella and McFarlane 1997), and third order (e.g., André et al.

Corresponding author address: Dr. Stéphane Bélair, Recherche en Prévision Numérique, 2121 Trans-Canada Highway, Room 500, Dorval, PQ H9P 1J3, Canada.
E-mail: stephane.belair@ec.gc.ca

1978; Moeng and Randall 1984). [The order of the turbulence closures refers to the highest turbulent moment predicted prognostically; see Stull (1988) and Holt and Raman (1988) for more details.] These schemes, particularly those with higher-order closures, have demonstrated some success in representing certain aspects of the evolution of daytime and nocturnal boundary layers. The local nature of these schemes does not allow them to represent the effects of the larger energy-containing eddies that often dominate the evolution of convective well-mixed layers. Thus, these schemes may not be appropriate for simulating buoyancy-driven convective PBLs that are evolving rapidly (Ebert et al. 1989; Holstlag and Moeng 1991; Chrobok et al. 1992).

In nonlocal approaches, the mixing that results from larger turbulent eddies is taken into account, leading to a better representation of convective well-mixed layers. For instance, the turbulent transilient theory (Stull 1984, 1993) was shown by Stull and Driedonks (1987) and Zhang and Stull (1992) to reproduce the structure and evolution of convective layers observed during field experiments. Other nonlocal techniques also were applied to convective PBLs, such as top-down bottom-up diffusion (Wyngaard and Brost 1984), spectral diffusivity theory (Berkowicz 1984), and integral turbulence closure (Fiedler and Moeng 1985). Unfortunately, the inclusion of these turbulence schemes into atmospheric models causes a considerable increase in computing time, prohibiting their use for many numerical applications.

To keep the computational cost at a reasonable level, some nonlocal effects have been introduced in a simpler fashion into turbulence schemes based on eddy diffusivity coefficients. The most popular method, proposed by Deardorff (1972), is to include countergradient (also called nonlocal) terms in the K (exchange coefficient) equations for turbulent fluxes of heat and moisture (see Mailhot and Benoit 1982; Therry and Lacarrère 1983; Troen and Mahrt 1986). The main effect of this modification is to allow for turbulent fluxes of heat and moisture to occur even in slightly upgradient situations; this approach was shown to help to represent better the convective PBLs (Holtslag and Boville 1993; Holtslag et al. 1995; Lüpkes and Schlünzen 1996).

Another approach for including nonlocal features into K-coefficient turbulence schemes was proposed by Bougeault and André (1986) and Bougeault and Lacarrère (1989). In their method, the mixing length at one level is derived from potential upward and downward displacements that could be achieved by parcels having kinetic energy equal to the mean turbulent kinetic energy (TKE) at that level, before being stopped by buoyancy effects. One advantage of this technique is it accounts for the vertical stability over the entire PBL. Despite its relative simplicity, this TKE-based approach incorporating some nonlocal effects has been shown by Cuxart et al. (1994) and Alapaty et al. (1997) to perform as well as more sophisticated schemes such as the transilient turbulent theory, at least for convective cases observed during the Hydrological Atmospheric Pilot Experiment-Modélisation du Bilan Hydrique (André et al. 1986) and First International Satellite Land Surface Climatology Project Field Experiment (Sellers et al. 1988) experiments.

In this study, we take advantage of the extensive aircraft measurements acquired during the Montreal-96 Experiment on Regional Mixing and Ozone (MERMOZ) that took place during summer 1996 (Mailhot et al. 1998), to verify and to improve a TKE-based turbulence scheme used in both the regional and global versions of the Canadian Meteorological Centre (CMC) operational model. More specifically, we want to evaluate the impact of including in this scheme some nonlocal features (such as those described above) on the simulation of two clear convective PBLs observed during MERMOZ. Because of its focus on aircraft measurements of turbulent quantities, complemented by a surface-based network that includes wind profilers and radiosondes, the MERMOZ experiment is well suited for this verification.

The two clear cases, carefully chosen to facilitate the comparison of model results with observations, exhibit quite different evolutions of their convective PBLs, as a result of the differing environment in which they occurred (see section 2). The performance of the TKE-based turbulence scheme in simulating these PBLs is evaluated in the context of the three-dimensional atmospheric Mesoscale Compressible Community (MC2) model (Benoit et al. 1997), which includes a detailed treatment of surface processes whose initial conditions (soil water content and surface temperature) were calibrated so as to minimize the errors on the low-level air temperature and humidity (see section 3). The evaluation is performed on the original configuration of the TKE scheme (section 4) and on versions that include countergradient terms and nonlocal mixing lengths (section 5).

2. Clear cases from MERMOZ

The MERMOZ field experiment (Mailhot et al. 1998) was conducted in the greater Montreal area during the period 3–28 June 1996 (see Fig. 1). The National Research Council (NRC) Twin Otter aircraft was flown over the area for a total of 24 flights. To facilitate the comparison of model results with observations, cases in which complicated processes (such as cloud, orographic, or lake effects) could have played a nonnegligible role in the development of the daytime convective PBL were eliminated. Using crew observations, surface insolation, satellite imagery, videotapes, and the CMC meteorological analyses, it was determined that the two best clear cases of the experiment were 15 and 28 June 1996.

The location of the lines flown during these two flights is shown in Fig. 1, as are the components of the

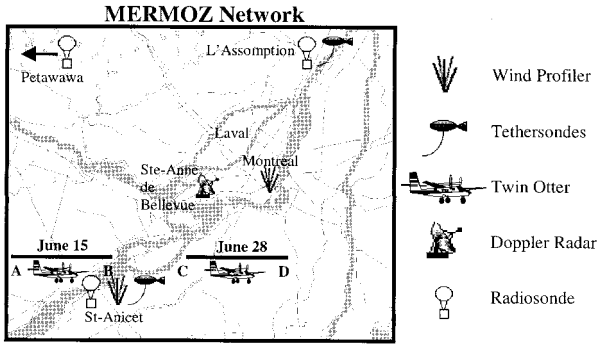

FIG. 1. Observational domain for the MERMOZ experiment. The locations of the wind profilers (at Montreal and St-Anicet), tethersondes (at L'Assomption and St-Anicet), Doppler radar (at Ste-Anne de Bellevue), and radiosondes (at L'Assomption, St-Anicet, and Petawawa) are indicated. The lines flown by the Twin Otter aircraft on 15 and 28 Jun also are shown.

complementary surface-based observational network. For quality control purposes, the airborne measurements were done with at least two different instruments on board the aircraft for each atmospheric variable and were compared with data from other sources such as radiosondes, tethersondes, and wind profilers. In general, the measurements from the various sensors agreed relatively well, as will be shown below.

The turbulent fluxes and statistics derived from the aircraft flights for these two cases are summarized in Table 1. The PBL or inversion height z_i was determined from temporal interpolation to the time of the flux runs using the soundings flown in each flight. (Note that z_i is defined in Table 1 as the height of the well-mixed layer and does not include the entrainment zone.) The TKE and vertical fluxes of heat H and latent heat LE have been computed using eddy correlation with high-pass-filtered time histories. Table 1b also includes the usual scales of friction velocity u_*, convective velocity w_*, and the stability parameter $-z_i/L$ (see, e.g., Moeng and Sullivan 1994), where L is the Obukhov length. Both cases exhibit several well-known observed features of convective PBLs [defined as PBLs that have $-z_i/L > 4.5$; e.g., Moeng and Sullivan (1994)], with a well-mixed layer, an active entrainment zone, and a marked capping inversion (e.g., Stull 1988). However, the two cases evolved quite differently because of the environments in which they occurred.

a. The 28 June 1996 case

The synoptic atmospheric conditions at 1200 UTC 28 June (all times are in UTC; EDT = UTC − 4 h), depicted in Fig. 2a, were conducive to clear skies over the MERMOZ project area. Indeed, both the position of the surface high pressure perturbation and the divergent low-level flow indicate large-scale subsidence over this region. These conditions were responsible for what turned out to be the clearest day of the experiment, with only a few scattered boundary layer clouds over western Quebec, far from where aircraft measurements were taken (along line C–D in Fig. 1).

TABLE 1a. Turbulence statistics and parameters derived from aircraft measurements. Times refer to beginning of flight legs.

Time (UTC)	z (m)	z_i (m)	TKE (m^2 s^{-2})	$(\overline{u'w'})$ (N m^{-2})	$(\overline{w'\theta'})$ (W m^{-2})	$(\overline{w'q'})$ (W m^{-2})
15 Jun 1996						
1714	319	1000	1.17	−0.18	47	234
1724	604	1060	1.20	−0.11	39	156
1736	872	1140	1.71	−0.17	17	263
1755	172	1260	1.89	−0.34	89	289
1808	458	1340	1.78	−0.25	79	185
1818	735	1400	2.07	−0.32	62	490
1830	1041	1475	2.17	−0.09	−20	257
28 Jun 1996						
1655	162	830	1.44	−0.19	125	437
1707	440	875	1.30	−0.04	38	570
1719	716	910	1.16	−0.03	22	654
1735	302	950	1.30	−0.02	72	257
1747	561	990	1.48	−0.14	27	694
1759	165	1045	1.50	0.02	95	384
1822	450	1145	1.88	−0.24	79	489
1834	871	1215	1.57	0.01	27	379

TABLE 1b. Additional aircraft-derived parameters.

Time (UTC)	z_i (m)	$-z_i/L$	w_* (m s^{-1})	u_* (m s^{-1})
15 Jun 1996				
1730	1080	8	1.5	0.6
1820	1425	6	1.8	0.7
28 Jun 1996				
1720	910	15	1.7	0.5
1815	1100	9	1.8	0.6

A series of eight 30-km flux runs were performed along line C–D by the aircraft (Fig. 3a), and four vertical soundings were performed over point C or D. The vertical structures of potential temperature θ, specific humidity q_v, and wind speed $|V| = (u^2 + v^2)^{1/2}$ (where u and v are the E–W and N–S components of the horizontal wind velocity) for the soundings S1, S3, and S4 (all at point D) are shown in Fig. 4. Early in the afternoon (1645 UTC), a well-mixed layer extends to about 800 m. It is capped by a shallow inversion layer and a deeper mixed layer reaching up to 1100 m (the remnants of the previous day's PBL). The mixed layer has increased to about 1300 m two hours later (1845 UTC), after having grown into the upper-level mixed layer. The entrainment zone is about 300 m thick. During this vertical growth, the well-mixed layer warmed by 2–3 K and dried by about 1 g kg^{-1}. In agreement with the large-scale analyses, the winds are quite weak, that is, 2–3 m s^{-1} in the PBL, increasing to 4–5 m s^{-1} in the free atmosphere aloft.

Clearly, horizontal advection processes do not play a major role in this case because low-level winds are weak. Also, boundary layer turbulence is generated mainly by buoyancy since there is almost no wind shear in the PBL and in the entrainment zone. With $-z_i/L \sim$

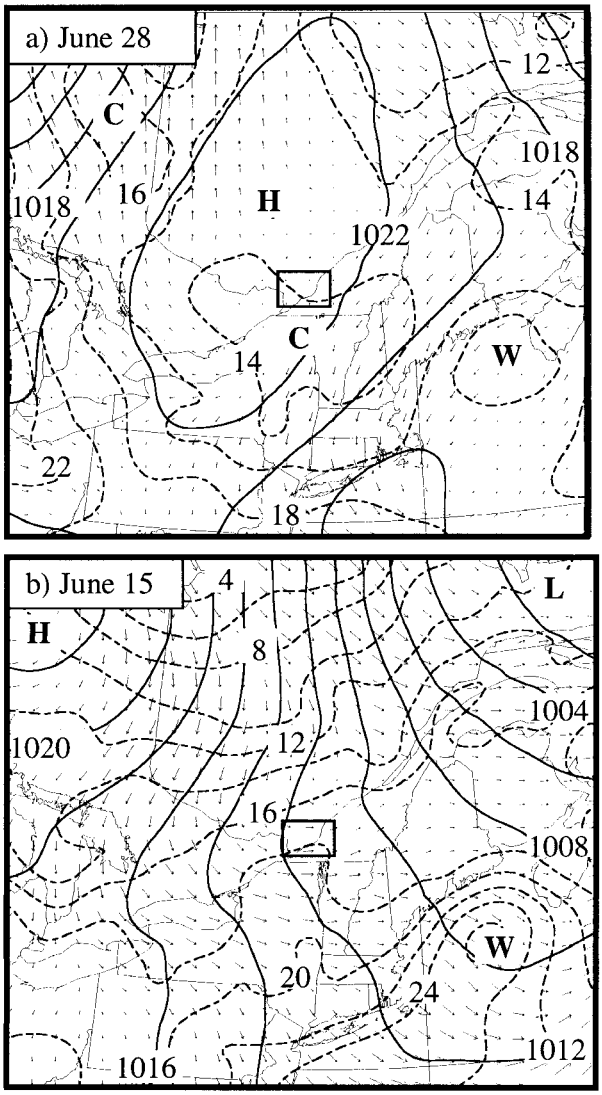

FIG. 2. Synoptic situations valid at (a) 1200 UTC 28 Jun 1996 and (b) 1200 UTC 15 Jun 1996. The surface winds, sea level pressure (in hPa), and surface air temperature (°C) are shown. The letters ''H'' and ''L'' are for high and low pressure centers, whereas the letters ''W'' and ''C'' are for warm and cold centers, respectively. The MERMOZ observation domain (see Fig. 1) is indicated by the small boxes in the Montreal area.

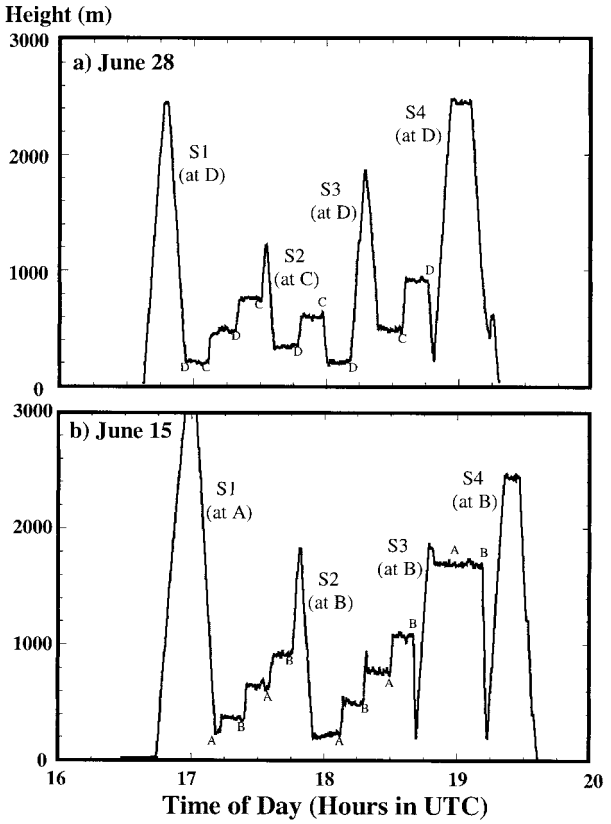

FIG. 3. Time–height flight patterns flown on (a) 28 Jun and (b) 15 Jun by the NRC Twin Otter aircraft. The end points (letters ''A,'' ''B,'' ''C,'' and ''D''; see Fig. 1) are indicated, as well as the locations and times of the soundings.

10, this case exhibits many features typical of the strongly convective regime (e.g., Moeng and Sullivan 1994), such as well-mixed and light winds in the PBL with an increase near the PBL top (Fig. 4) and profiles of TKE that are almost constant with height (Table 1 and Fig. 9, which is described in section 4).

Reflectivities from the wind profiler at St-Anicet are shown in Fig. 5a. Note that no returned power signal was received for a few hours during the afternoon (from about 1600 to 1900 UTC) because the profiler was used in radio acoustic sounding system (RASS) mode during that time. The height of the mixed layer at 1900 UTC, indicated by the strong signal at the top of the layer caused by the abrupt changes in the refraction index, is very similar to that derived from aircraft soundings (i.e., 1300 m).

b. The 15 June 1996 case

In contrast to 28 June, atmospheric conditions were not as simple for the 15 June case. In the morning hours preceding the flight, a fast-moving low-level cold front passed over the MERMOZ area, producing clouds that cleared only a few hours before aircraft measurements were taken. (This baroclinic region, which was slightly upwind of Montreal early in the morning at 1200 UTC, can be seen in Fig. 2b.) Thus, the flight on 15 June was performed in the cold and clear air behind the front where strong northwesterly winds were responsible for significant cold advection (Fig. 2b). In the last few runs of the flight, small fair-weather cumulus clouds started to develop along the western portion of line A–B (see Fig. 1), changing the nature of the flight. Because of this change, care has been taken to consider only the earlier measurements from the period of clear conditions for the comparison against model outputs. The flight

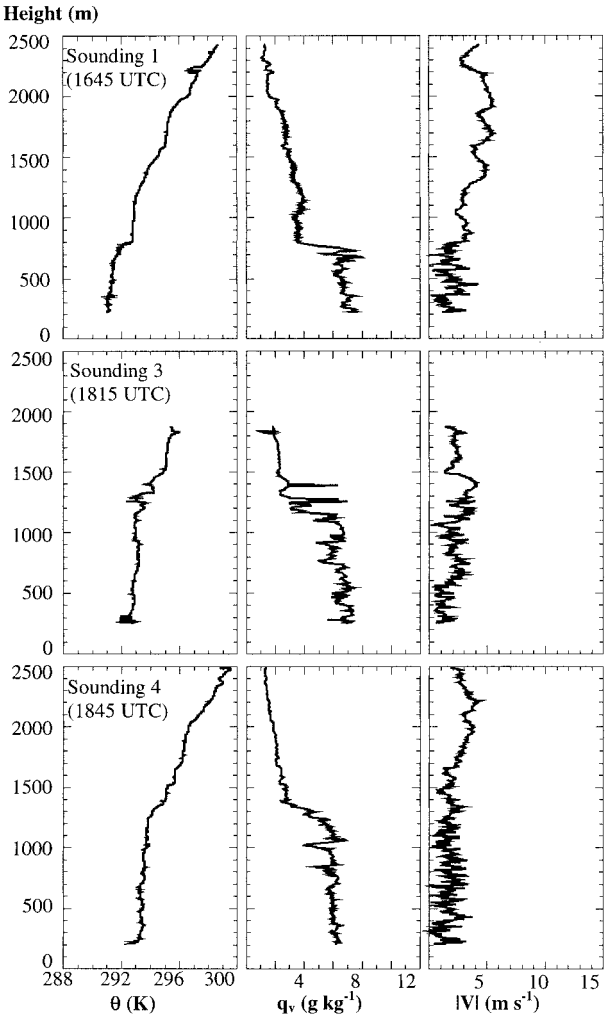

FIG. 4. Aircraft-measured soundings for the flight on 28 Jun 1996. The potential temperature (K), specific humidity (g kg^{-1}), and wind speed (m s^{-1}) are shown as a function of height (m). The sounding number refers to the labeling shown in Fig. 3. The central time of the observation period is indicated for each sounding.

pattern on 15 June was very similar to that flown during 28 June, with nine flux runs and four vertical soundings (see Fig. 3b). The last two flux runs encountered clouds and were not considered for model verification. The last soundings of the flight, however, were kept in the analysis since they were performed in the clear portion of the line (at point B).

Wind profiler and aircraft measurements (Figs. 5 and 6) both indicate that the convective PBL deepened rapidly on 15 June, with a well-mixed layer of about 1200 m at 1745 UTC, 1500 m at 1835 UTC, and 1900 m at 1910 UTC (i.e., an increase of 700 m in less than 1.5 h). Although the data from these soundings only represent point measurements of a variable PBL at different times, inspection of the PBL tops indicated by the other aircraft soundings revealed a consistent picture of a continually deepening PBL, such that this rapid increase could not be attributed to a statistical measurement error. The warming and drying associated with the vertical expansion were not as important as for the 28 June case, and the well-mixed layer was cooler and more humid.

The greatest difference between the boundary layers observed during the two cases is in the vertical structure of the horizontal winds. Clearly, the winds were more intense on 15 June, both in the well-mixed layer and in the free atmosphere above. As shown in Fig. 6, the vertical wind shear at the top and above the well-mixed layer is larger during 15 June, at least in the earlier stages of the PBL development (at 1910 UTC the winds in the mixed layer have increased because of deep vertical mixing so that the vertical wind shear has disappeared almost completely at that time). This observation suggests a potentially more important role of wind shear–related mechanisms in the generation of turbulence, which could contribute to the faster PBL evolution observed in this case. The effects of the wind shear also can be seen in the TKE profile (Table 1 and Fig. 11, which is described in section 4) with local generation of TKE near the PBL top, a feature that also is apparent in the intermediate type of PBL (where both shear and buoyancy forcings are important) studied by Moeng and Sullivan (1994; e.g., their Figs. 19 and 24). Therefore, this case corresponds to a moderate convective regime with strong winds and shear-driven effects near the PBL top.

There is no doubt that the simulation of the 15 June PBL represents a greater challenge than that observed on 28 June, because of complicating factors such as the greater vertical wind shear, horizontal advection, and the morning clouds. This case is probably more representative of real weather situations, which invariably are more complex than the almost-textbook situation that occurred on 28 June. Atmospheric models must be able to handle such cases. Therefore, we believe these two contrasting cases, when taken together, provide a good dataset to verify the performance of the turbulence scheme in varying environmental conditions.

3. Modeling system and setup

In this study, the verification of the TKE-based turbulence scheme is done with the MC2 model, as mentioned in section 1. Although this model is nonhydrostatic and could therefore be used for simulating very small-scale circulations, we chose to run it at the relatively coarse horizontal resolution of 35 km, which corresponds approximately to the length of the aircraft flux runs. The aircraft vertical soundings and turbulent fluxes are thus directly compared to simulated profiles at the nearest model columns. Since only a few model columns are used for the verification, the methodology adopted here for testing the turbulence scheme is not unlike using a 1D column model except, of course, that the full atmospheric 3D equations are solved (as compared to a simplified set of equations for column models)

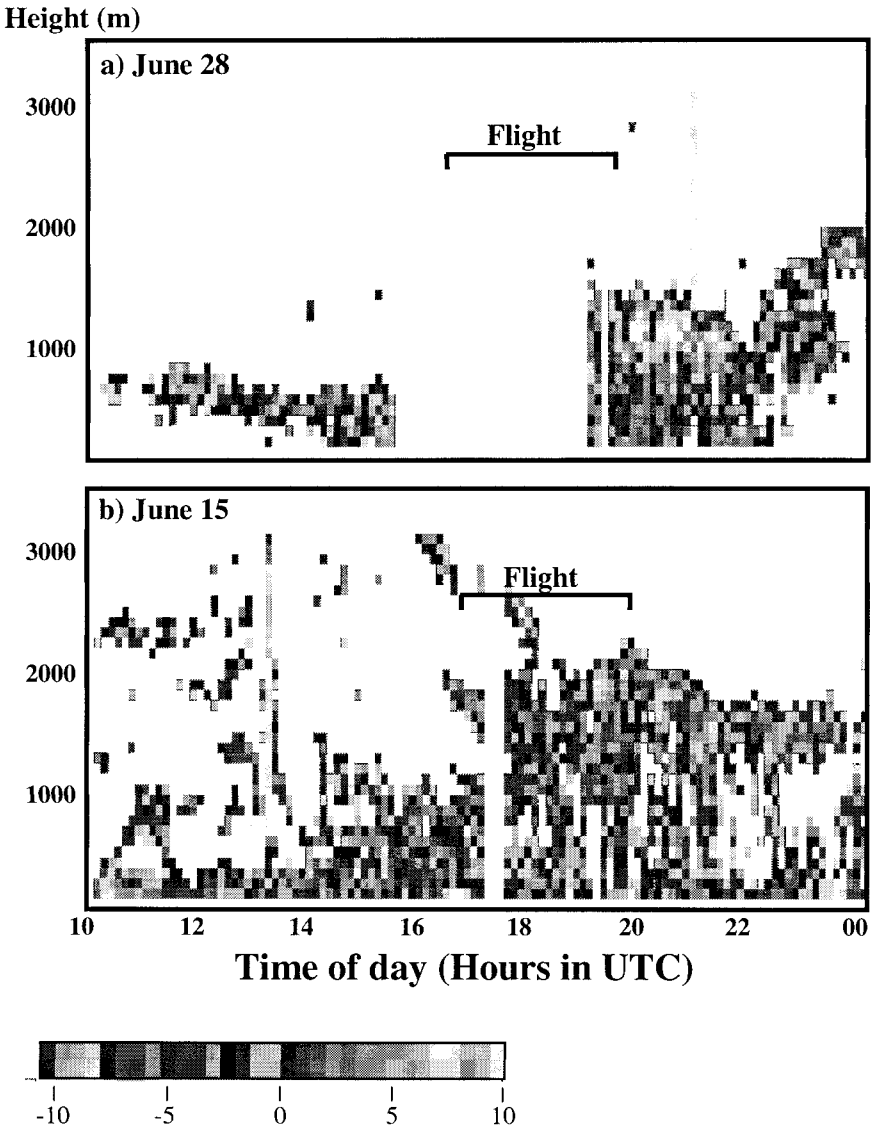

FIG. 5. Reflectivities of the 915-MHz Doppler wind profiler located at St-Anicet as a function of time and height. The time periods corresponding to aircraft measurements are indicated by brackets.

and horizontal effects such as advection are represented explicitly.

a. The MC2 model

In brief, MC2 is a limited-area model that integrates the 3D, nonhydrostatic, fully compressible Euler equations (see Tanguay et al. 1990), using finite differences and semi-implicit/semi-Lagrangian techniques for the spatial and temporal discretizations, respectively. The main dynamical and numerical features of MC2 are summarized in Table 2.

Together with the turbulence scheme, described in more detail in the next section, the model includes the main physical processes important for the evolution of the PBL. For instance, the surface fluxes of heat, moisture, and momentum are calculated using a force–restore technique in which a more realistic representation of vegetation has been included. This scheme, called Interactions between Soil, Biosphere, and Atmosphere (ISBA; Noilhan and Planton 1989), has been shown to represent adequately the exchanges between the surface and the atmosphere for various landscapes, timescales, and meteorological situations (e.g., Jacquemin and Noilhan 1990; Mahfouf and Jacquemin 1989). Radiative processes are computed with relatively sophisticated schemes for both infrared (Garand 1983) and solar (Fouquart and Bonnel 1980) radiation, each considering interactions with clouds, water vapor, ozone, and carbon dioxide. Condensation processes, less important in this

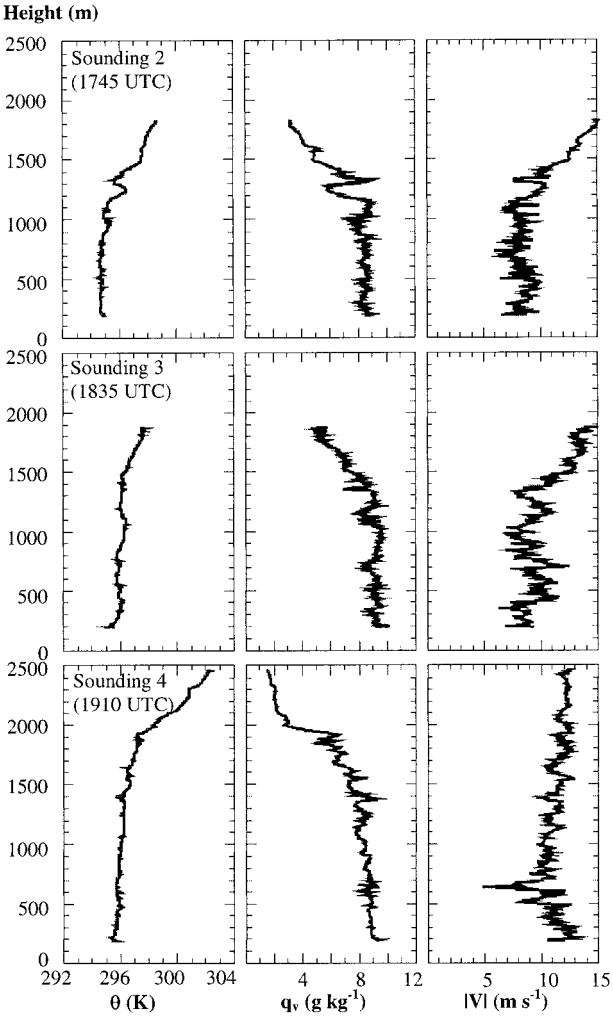

FIG. 6. Same as Fig. 4 but for the flight on 15 Jun 1996.

study because only clear cases are examined, are handled using a Kuo-type (1974) scheme for deep convection and a simple supersaturation removal scheme for grid-scale condensation.

For each of the two cases, the model was integrated from early morning (1200 UTC) to early evening (2100 UTC) using CMC's meteorological analyses for both initial and lateral boundary conditions. The horizontal domain covered by the 35-km grid is shown in Fig. 7. In the vertical, the adopted strategy consists in concentrating most of the levels in the lowest 3 km at a uniform resolution of 75 m, and then in slowly decreasing the resolution above that height until the top of the model (25 km above ground) is reached.

b. The turbulence scheme

In general, the diffusive tendencies resulting from turbulent mixing in the PBL can be written as

TABLE 2. Summary of MC2's dynamics and numerics.

- Fully compressible Euler equations
- Horizontal Cartesian coordinate on polar stereographic projection of sphere; vertical terrain-following (modified Gal–Chen) coordinate
- Helmholtz equation on perturbations of log[pressure($t + \Delta t$)]
- Nesting of lateral and upper boundaries for all prognostic variables (sponge zones)
- Variable resolution in the vertical
- Three time levels ($t - \Delta t$, t, $t + \Delta t$) plus filter plus off-centering
- Semi-implicit time scheme
- Three-dimensional semi-Lagrangian scheme
- Horizontal and vertical staggering with second-order finite differencing
- Implicit $2\Delta x$ filtering of topography due to horizontal staggering
- Time-implicit horizontal diffusion on horizontal and vertical velocity, temperature, pressure, and humidity

$$\frac{\partial X}{\partial t} = -\frac{1}{\rho}\frac{\partial}{\partial z}(\rho\overline{w'X'}), \tag{1}$$

where ρ is the air density, w is the upward velocity, t is time, z is height above ground, and X represents the atmospheric variables (θ, q_v, u, v). As usual, the overbars indicate temporal and spatial averaging and the primes denote deviations from such averages.

In MC2, the turbulent fluxes of heat, humidity, and momentum ($\overline{w'X'}$) are parameterized using eddy diffusivity coefficients K that directly depend on TKE (here also denoted as E) and on a turbulent mixing length λ:

$$\overline{w'X'} = -K_T\left(\frac{\partial X}{\partial z} - \Gamma_X\right) \quad \text{for } X = (\theta, q_v), \tag{2}$$

$$\overline{w'V'} = -K_M\left(\frac{\partial V}{\partial z}\right) \quad \text{for } V = (u, v), \tag{3}$$

$$K_M = a\lambda E^{1/2}, \quad \text{and} \quad K_T = \frac{K_M}{\text{Pr}}, \tag{4}$$

where K_T and K_M are the eddy diffusivity coefficients for temperature/humidity and momentum, respectively; a is a coefficient ($=0.516$); and Pr is the Prandtl number. In the current version of the scheme, the countergradient (or nonlocal) terms Γ_X are neglected ($\Gamma_X = 0$), so that upward fluxes ($\overline{w'\theta'} > 0$) can only occur for negative vertical gradients (i.e., $\partial X/\partial z < 0$).

The closure problem is therefore reduced to the determination of TKE and λ. For the evolution of TKE, the following prognostic equation is solved [see Mailhot and Benoit (1982) and Benoit et al. (1989) for more details]:

$$\frac{\partial E}{\partial t} = \underbrace{\frac{g}{\theta_v}(\overline{w'\theta_v'})}_{\text{B}} - \underbrace{\overline{w'V'}\frac{\partial V}{\partial z}}_{\text{M}} + \underbrace{\frac{\partial}{\partial z}\left(K_M\frac{\partial E}{\partial z}\right)}_{\text{T}} - \underbrace{c\frac{E^{3/2}}{\lambda_\epsilon}}_{\text{D}}, \tag{5}$$

in which θ_v is the virtual potential temperature, g is the

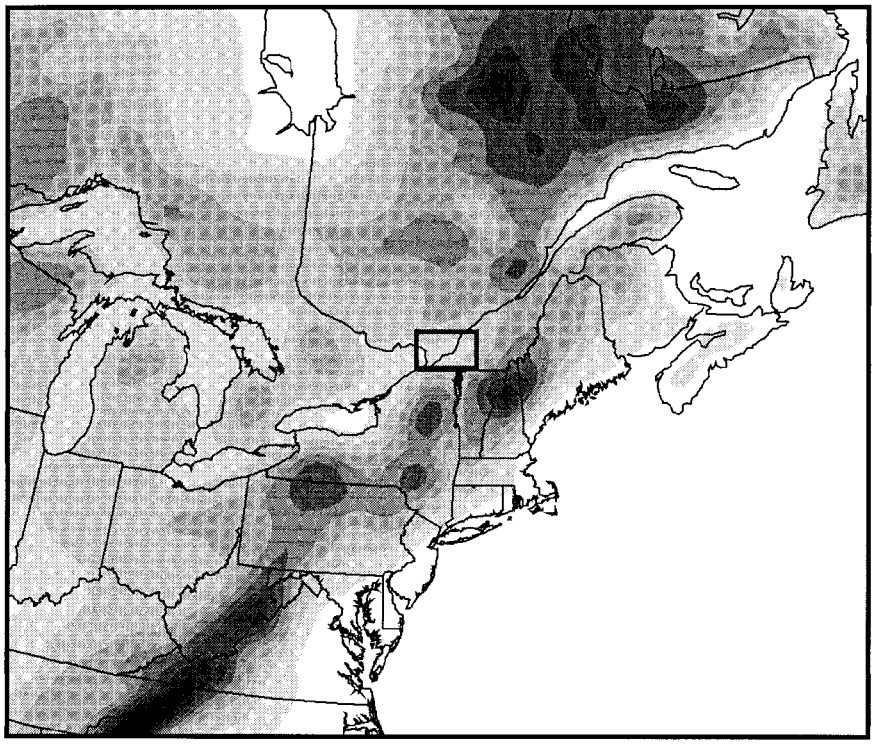

FIG. 7. The 35-km resolution integration domain of the MC2 model. Shadings represent the terrain elevation (every 100 m). The observational domain of the MERMOZ experiment (see Fig. 1) is indicated by the thick box in the Montreal area.

acceleration of gravity, c is a parameter, and λ_ϵ is a dissipation length scale. The advection of TKE is not considered in this equation, but mechanisms such as the generation of turbulence due to buoyancy and vertical wind shear (terms B and M) and the vertical redistribution and dissipation of TKE (terms T and D) are accounted for in calculations of the K coefficients.

On the other hand, λ is given by the ratio λ_n/φ_M, in which λ_n is a mixing length in statically neutral conditions (relaxed toward an equilibrium profile that increases linearly with height—following kz, k being the von Kármán constant—from zero at the ground to the asymptotic value of 200 m), and φ_M is a stability function depending on the local Richardson number:

$$\mathrm{Ri} = \frac{g}{\theta_v} \frac{\dfrac{\partial \theta_v}{\partial z}}{\left(\dfrac{\partial u}{\partial z}\right)^2 + \left(\dfrac{\partial v}{\partial z}\right)^2}. \quad (6)$$

For an unstable stratification ($\mathrm{Ri} < 0$),

$$\varphi_M^2 = (1 - 40\mathrm{Ri})^{-1/3}. \quad (7)$$

For a stable stratification ($\mathrm{Ri} > 0$),

$$\varphi_M = (1 + 12\mathrm{Ri}). \quad (8)$$

These formulations are further described in Delage and Girard (1992) (for the unstable case) and in Delage (1997) (for the stable case). Note also that λ_ϵ in Eq. (5) is currently taken as equal to λ.

Perhaps the main advantage of this type of boundary layer formulation is it remains relatively simple while considering the main physical processes occurring in the PBL. Note, however, that in its current form this scheme is entirely ''local,'' since the vertical diffusion coefficients at one level depend only on atmospheric variables (and their vertical gradients) at that level. In the next sections, we evaluate the performance of this scheme for convectively unstable PBLs and examine the impact of including some nonlocal features such as the countergradient terms in Eq. (2) and more sophisticated calculations for the turbulent mixing and dissipation lengths.

c. Calibrations

Because of the complexity of the physical processes involved in the daytime evolution of the boundary layer, one must be careful when comparing model-simulated PBLs against observations. First, the initial conditions of the model have to be as realistic as possible and include features such as low-level stable layers, residual mixed layers, and free-atmosphere inversions, if observed. Also, since the heat and momentum surface fluxes are known to have a substantial impact on the diurnal evolution of the PBL, it is important to ensure that the

surface energy budget is well represented. In particular, the solar energy reaching the surface and its partitioning into latent, sensible, and ground heat fluxes have to be correct.

For the initial conditions, vertical profiles from radiosondes launched early in the morning (1200 UTC) at St-Anicet, Maniwaki (northwest of the MERMOZ region), and Petawawa were used to verify the early stages of the simulated PBL. The initial PBL was well simulated for the 28 June case, but the lowest few kilometers were too humid (by 1–2 g kg^{-1}) for the 15 June case. This discrepancy between the observations and analysis was removed by reanalyzing in a more local manner the upwind soundings from Maniwaki and Petawawa, following the simple objective analysis technique of Barnes (1964).

Similarly, the simulated solar radiation reaching the surface was compared to detailed radiometric measurements at St-Anicet and L'Assomption, and was found to be larger than the observed values by about 100–200 W m^{-2} in both cases. This overestimation, possibly due to an overly simple treatment of atmospheric aerosols in MC2, was corrected in a crude manner by simply adjusting the solar downward radiation at the surface so as to fit the observations.

The partitioning of the available energy at the surface (incident radiation minus reflected) among sensible, latent, and ground heat fluxes mostly depends on the types of soil and vegetation and on the soil moisture content. In this study, special care was taken to construct a vegetation field that is as realistic as possible using the 1-km United States Geological Survey database. Unfortunately, the soil type could not be as well specified because of a lack of high-resolution data for the MERMOZ region. Consequently, an intermediate type of soil between sand (coarse) and clay (fine) was chosen for the entire integration domain. This simplification is of small consequence since the surface scheme ISBA is not as sensitive to soil types as it is to vegetation, at least for short-range simulations, provided that the relative soil humidity is well initialized.

The important task of initializing or calibrating the initial surface temperature and humidity is handled by a sequential assimilation technique elaborated by Mahfouf (1991) and later refined by Bouttier et al. (1993). According to this method, briefly described in appendix A, corrective increments to the initial soil moisture and surface temperature are applied through successive simulations in order to minimize the errors in the low-level air temperature and humidity at 1800 UTC (i.e., in mid-afternoon). It is important to note that this calibration does not force the simulated surface fluxes toward observed values (since we do not know a priori the surface fluxes), but rather forces them to be of the right amplitude to generate air temperature and relative humidity that agree well with meteorological observations. It will be shown that it is quite possible to obtain reasonable vertical temperature and humidity profiles in the PBL even though the surface and turbulent fluxes are quite different from observations.

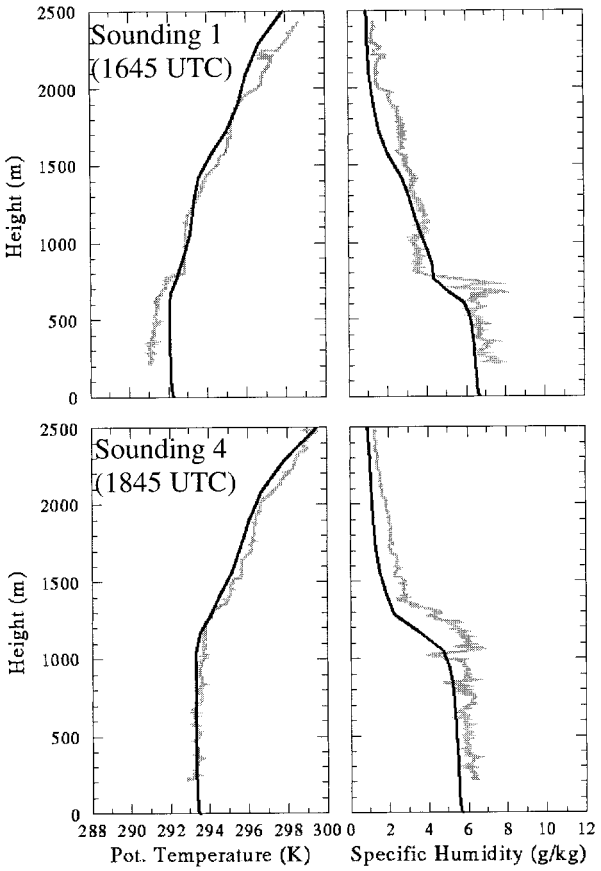

FIG. 8. Comparison of observed (gray) and simulated (black) potential temperature (K) and specific humidity (g kg^{-1}) profiles for the local simulation for 28 Jun 1996. Results from the two nearest grid points are used for the simulated profiles.

4. Results with the local formulation

In this section, the vertical structures and turbulent fluxes that result from the simulations of the two clear PBLs using the local formulation described in section 3b are examined and compared against aircraft measurements. In both cases, two measured θ and q_v soundings, taken at the same end points of the flux lines (point D for 28 June and point B for 15 June; see Fig. 1), are compared with model profiles averaged over the two nearest grid points. Similarly, aircraft-measured turbulent quantities [TKE, $H = \rho c_p(\overline{w'\theta'})$, LE $= \rho L(\overline{w'q_v'})$, where c_p is the specific heat capacity of air and L is now the latent heat of vaporization] are plotted against four-point model averages at the central time of two observation periods—one for the first half of the flight and one for the second half.

The results for 28 June are shown in Figs. 8 and 9. Note the good agreement between the observed and simulated low-level air temperature and humidity in Fig.

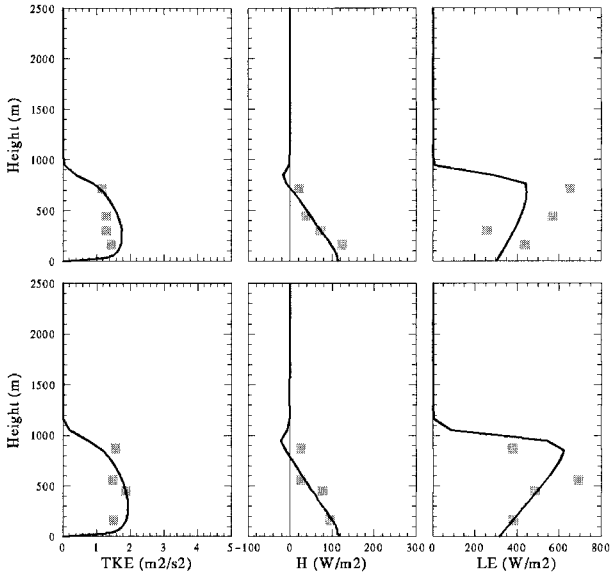

FIG. 9. Comparison of observed (gray squares) and simulated (lines) turbulent kinetic energy (TKE, $m^2\ s^{-2}$) and turbulent fluxes of sensible (H, W m^{-2}) and latent (LE, W m^{-2}) heat for the local simulation for 28 Jun 1996. The observational period is divided in two: one centered at 1720 UTC (top) and one at 1815 UTC (bottom). Results from the four closest grid points are used for the simulated turbulent quantities.

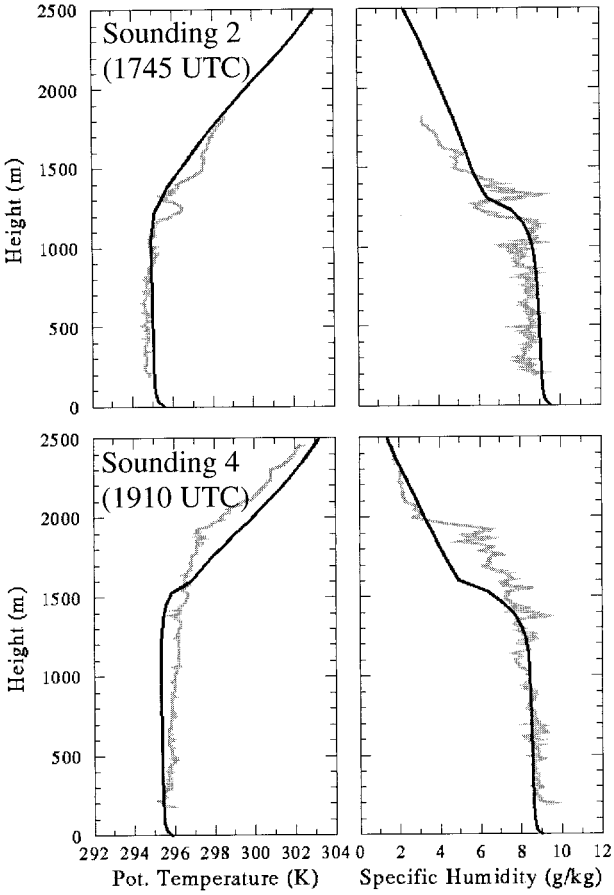

FIG. 10. Same as Fig. 8 but for the local simulation for 15 Jun 1996.

8. This agreement is not surprising since the initial values of the surface prognostic variables were calibrated to minimize the low-level errors at 1800 UTC. Likewise, the rest of the simulated PBL agrees fairly well with observations, with a warming and drying well-mixed layer that deepens from a thickness of about 700 m at 1645 UTC to 1100 m at 1845 UTC. The few discrepancies with the observations such as the smoother transition between the well-mixed and free atmosphere, the slight vertical instability ($\partial\theta/\partial z < 0$) in the well-mixed layer, and the weak underdevelopment of the well-mixed layer are not critically important.

Remarkably, the turbulent fluxes of sensible (H) and latent (LE) heat necessary to generate this evolution of the boundary layer compare quite well with the aircraft flux measurements (see Fig. 9). The simulated H fluxes decrease linearly with height from about 120 W m^{-2} at the surface to -20 W m^{-2} at the inversion, whereas the LE fluxes increase from a value of about 300 W m^{-2} at the surface to 600 W m^{-2} just below the inversion, indicating that the mixed layer is warming and drying. The negative H fluxes and large positive LE fluxes in the entrainment zone occur because cooler (low θ) and moister PBL air is pushed upward in the free atmosphere, while warmer (high θ) and drier air from above is entrained downward in the PBL. For both the model results and observations, the turbulence intensity, indicated by TKE, is mainly constant throughout the PBL, with values of about 1.5–1.75 $m^2\ s^{-2}$. Considering that uncertainties related to aircraft measurements of turbulent fluxes could be on the order of 20%–30% (see Lenschow and Stankov 1986), the model captures very well the turbulent structure of the PBL for this strongly convective case.

Unfortunately, the evolution of the PBL observed during 15 June is not as well represented by the model, as shown in Figs. 10 and 11. Even though the simulated and observed PBLs agree almost perfectly at 1745 UTC (note again the good simulation of low-level temperature and humidity due to the calibration mechanism for the surface variables), the model clearly fails to reproduce the rapid deepening of the well-mixed layer that occurred in the following 85 min (see Fig. 10). At 1910 UTC, the depth of the simulated well-mixed layer is about 1500 m as compared to 1900 m for the observations, indicating observed growth rates more than twice as fast as those simulated [i.e., 700 m $(85\ min)^{-1}$ vs 300 m $(85\ min)^{-1}$]. The largest difference is found in the vertical extent of the entrainment zone which is much too shallow in the simulation, indicating a lack of turbulence generation in that layer.

This discrepancy is surprising if we consider that the simulated turbulence intensity and sensible heat fluxes already necessary to generate this slower evolution are much larger than those observed (see Fig. 11). This fact

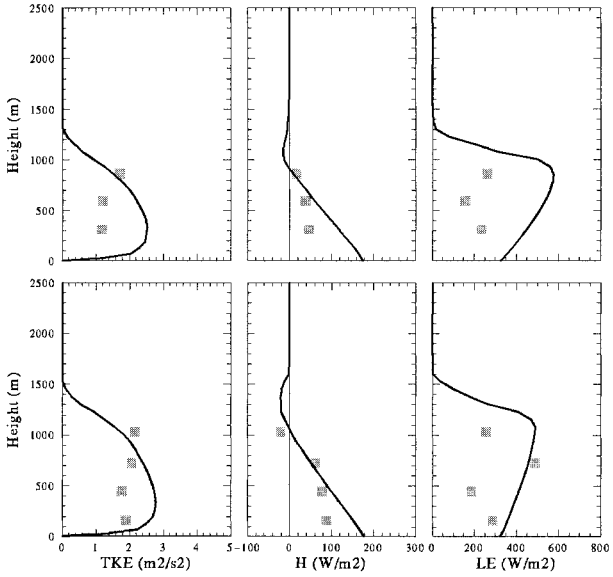

FIG. 11. Same as Fig. 9 but for the local simulation for 15 Jun 1996. The two observational periods are centered at 1730 UTC (top) and at 1820 UTC (bottom).

is particularly true in the lowest portion of the PBL, where the simulated TKE is about 2.4–2.8 $m^2 s^{-2}$, compared to the smaller observed values of 1.2–2.0 $m^2 s^{-2}$, and where the simulated *H* fluxes are almost twice as large as aircraft observations (at the surface, the simulated *H* flux is about 180 W m^{-2} while observations suggest values closer to 100 W m^{-2}). In the upper portion of the PBL, unfortunately, detailed aircraft measurements are not available to reveal the intensity of turbulence in the entrainment layer. But the slight increase of TKE with height observed for both periods suggests that while overpredicting turbulence in the lower PBL, the model may be underpredicting the turbulence near the inversion, resulting in an underestimation of the entrainment. The weak negative *H* fluxes (~ -20 W m^{-2}) in the entrainment zone also indicate that entrainment was small in the simulation (but again no observations were collected to confirm this hypothesis).

It is likely that this underprediction of entrainment is responsible for the slower evolution of the simulated PBL for the 15 June case. Obviously, the environmental conditions observed during this particular case, including the wind shear near the top of the PBL and the cold air advection, could have promoted entrainment and favored a rapid growth of the PBL. Yet, these environmental conditions were found to be well represented by the model—as well as is possible, of course, for a 35-km mesoscale model with a 75-m vertical resolution. It is therefore our opinion that the poor representation of the 15 June PBL should be attributed, at least in part, to imperfections in the formulation of the turbulence scheme.

Previous studies have reported difficulties for local *K* schemes to represent fast-evolving convectively unstable PBLs (see Ebert et al. 1989; Chrobok et al. 1992), which were attributed to the larger turbulent eddies with mixing effects that are felt throughout the whole depth of the PBL, not just locally. In an attempt to include such effects, nonlocal features have been added in the turbulence scheme and their impact on the simulation of both cases is evaluated in the next section. While special attention will be given to the more difficult case of 15 June, we also must verify that the excellent results obtained for 28 June do not deteriorate due to the inclusion of nonlocal features.

5. Results with nonlocal formulations

Examining the local formulation described in section 3b, one finds that there are at least two ways to include nonlocal features in the current boundary layer scheme. A first strategy consists of directly inserting nonlocal (or countergradient) terms Γ_X in Eq. (2) for the turbulent fluxes of heat (and possibly moisture). As discussed in the next section, the improvement resulting from this term is marginal. Another method, which will be shown to have a greater impact on the results, is to modify the eddy diffusivity coefficients in Eq. (4) by using a different approach for calculating the turbulent lengths λ and λ_ϵ. Descriptions of these strategies, as well as results, are given in the remainder of this section.

a. Nonlocal (countergradient) terms

Nonlocal terms of the type introduced by Deardorff in the early 1970s have since been used in a large number of turbulence schemes, as exemplified by the noncomprehensive list given in Table 3. For simplicity, only the countergradient term for sensible heat fluxes (i.e., Γ_θ) is examined in this study. The purpose of this term is to represent the effect of buoyant plumes in the well-mixed layer by simply forcing a positive (upward) background flux $[(\overline{w'\theta'})_{BG} = K_T\Gamma_\theta]$ that depends on nonlocal quantities such as the kinematic surface heat flux $(\overline{w'\theta'})_s$ or the inversion height. The main effect of this background flux is to allow for positive turbulent heat fluxes even in weakly stable stratification. As noted by Holtslag and Moeng (1991), the nonlocal term is important in the bulk of the PBL while the local term contributes mostly near the surface and at the inversion, where larger gradients of θ are found.

All the nonlocal formulations listed in Table 3 were tested in this study. Since the results were almost identical for each of them, only the simulated profiles obtained using the most recent formulation (i.e., based on Holtslag and Moeng 1991) are shown in Fig. 12. Clearly, very few differences are found between profiles from the local (dashed lines) and nonlocal (full lines) simulations. The boundary layer profiles of θ and q_v are slightly more stable and less well mixed when using the nonlocal term, but this improvement is marginal com-

TABLE 3. Nonlocal term formulations. Note: subscripts "0" and "S" refer to low-level and surface values, respectively.

Formulation	Notes	References
$\Gamma_\theta = 0.7 \times 10^{-3}$ K m^{-1}		Deardorff (1966)
$\Gamma_\theta = \dfrac{C(\overline{w'\theta'})_s}{w_* z_i}$	$C = 10$	Troen and Mahrt (1986)
	z_i = height of the inversion	Mailhot and Benoit (1982)
	$w_*^3 = \dfrac{g}{\theta_v}(\overline{w'\theta'_v})_s z_i$	
$\Gamma_\theta = \dfrac{g}{\theta_0}\dfrac{\overline{\theta'^2}}{\overline{w'^2}}$	$\overline{\theta'^2} = 1.8\left(\dfrac{z}{z_i}\right)^{-2/3}\theta_*^2$	Deardorff (1972)
	$\overline{w'^2} = 1.8\left(\dfrac{z}{z_i}\right)^{2/3}\left(1 - 0.8\dfrac{z}{z_i}\right)^2 w_*^2$	Therry and Lacarrère (1983)
	$\theta_* = \dfrac{(\overline{w'\theta'})_s}{w_*}$	
$\Gamma_\theta = b\dfrac{w_*(\overline{w'\theta'})_s}{\overline{w'^2} z_i}$	$b = 2$	Holtslag and Moeng (1991)
	w_* and $\overline{w'^2}$ same as above	

pared with that obtained in previous studies such as Holtslag and Boville (1993) and Lüpkes and Schlünzen (1996). The small impact of the countergradient term is probably due to the relatively small surface heat fluxes [about 100–175 W m^{-2} as compared to approximately 500 W m^{-2} in Lüpkes and Schlünzen (1996)] and the deeper well-mixed layer (in excess of 1000 m) in the present cases.

b. Mixing length of Bougeault–Lacarrère

The current calculations of the mixing lengths λ and λ_ϵ (based on stability functions φ_M; see section 3b), while having the advantage of being simple and consistent for both the surface and convective layers (see Delage and Girard 1992), are based on *local* Richardson numbers and cannot therefore account for the effect of varying vertical stratification throughout the whole depth of the boundary layer. For this reason, the approach described in Bougeault and André (1986) and Bougeault and Lacarrère (1989) was included in the model and tested for the two case studies.

In this method, usually referred to as the Bougeault–Lacarrère (hereinafter referred to as BL) technique, the turbulent lengths λ and λ_ϵ at a particular level are determined from the potential upward and downward displacements (l_{up} and l_{down}) that parcels with kinetic energy equal to the mean TKE at the originating level could accomplish before being stopped by buoyancy effects. This method translates into the following equations for l_{up} and l_{down}:

$$\int_Z^{Z+l_{up}} \beta[\theta(Z') - \theta(Z)]\, dZ' = E(Z),$$

$$\int_{Z-l_{down}}^{Z} \beta[\theta(Z) - \theta(Z')]\, dZ' = E(Z), \quad \text{and}$$

$$l_{down} < Z, \tag{9}$$

where Z is the height of the initial level, E is the local TKE, and β is a constant buoyancy parameter ($=g/\theta_{vs}$, where θ_{vs} is the virtual potential temperature of air near the surface).

The averaging of l_{up} and l_{down} to obtain the two turbulent lengths is a delicate aspect of the BL method. Here we use the same strategy as that described in Bougeault and Lacarrère (1989), based on the physical fact that diffusion coefficients vary with the distance to solid surfaces while the typical scale of dissipative eddies does not necessarily do so. Thus, λ is forced toward the smaller of the two mixing distances, while λ_ϵ is a geometric average:

$$\lambda = \min(l_{up}, l_{down}); \qquad \lambda_\epsilon = (l_{up} l_{down})^{1/2}. \tag{10}$$

In a well-mixed PBL, the two turbulent lengths are very similar in the central portion of the layer (where $l_{up} \cong l_{down}$ but can be quite different near the upper and bottom edges of the PBL (where one of the two distances l_{up} or l_{down} is significantly larger than the other). In these parts of the PBL, λ_ϵ can be much larger than λ.

From Figs. 8 and 13 it is evident that inclusion of the BL calculations does not improve the simulation of the PBL observed during 28 June. At both 1645 and 1845 UTC, the simulated mixed layer extends higher than the observed one with the gap between observations and model results increasing with time, indicating that the simulated deepening rate between the two observation times is overpredicted. As could be expected, the TKE predicted by the model for this more rapid evolution is larger than what was observed, and this occurs for the whole depth of the PBL (see Fig. 14). Interestingly, the turbulent sensible heat fluxes are smaller than those from both observations and the local run (cf. Figs. 9 and 14), with much larger negative val-

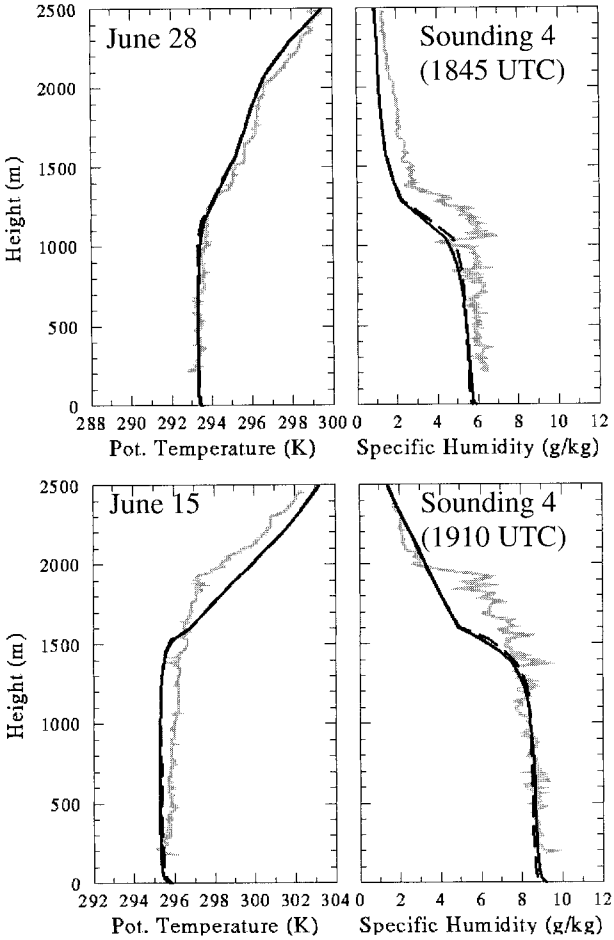

FIG. 12. Impact of including the nonlocal (countergradient) terms in the vertical turbulent fluxes as shown by comparison of simulated profiles of potential temperature (K) and specific humidity (g kg^{-1}) in the local (dashed) and nonlocal (full) simulations with observations (gray). The comparison is done for the last soundings performed on 15 and 28 Jun.

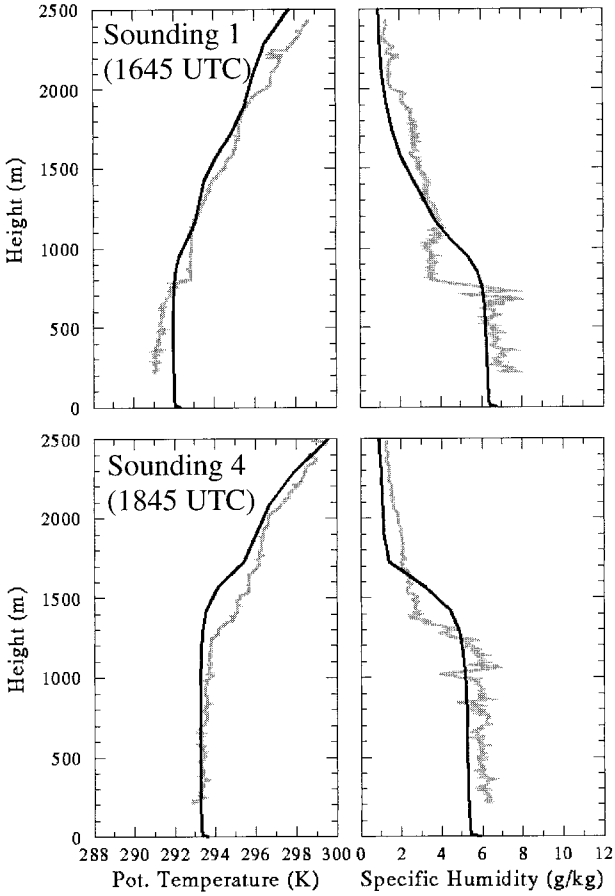

FIG. 13. Same as Fig. 8 but for the simulation using the BL turbulent scales, for 28 Jun 1996.

ues in the entrainment zone (~ -90 W m^{-2} at z_i). This behavior indicates that entrainment processes at the top of the boundary layer are possibly too active when using the BL turbulent lengths, and that, consequently, smaller turbulent heat fluxes are required to generate the same development of the boundary layer, as compared to those in the local formulation. For the present case, unfortunately, the deepening rate was overestimated and the heat fluxes were underestimated by the model. This result indicates that the BL turbulent lengths (either λ or λ_ϵ, or both) are possibly too large near the top of the PBL, resulting in excessive entrainment. Indeed, in a recent study using a large-eddy simulation model, Cuijpers and Holtslag (1998) examined prototype convective PBLs and noted that the BL formulation produces large length scales at the PBL top that result in too much entrainment.

For the 15 June case, the model with the BL turbulent lengths generates a very thick mixed layer at 1910 UTC,

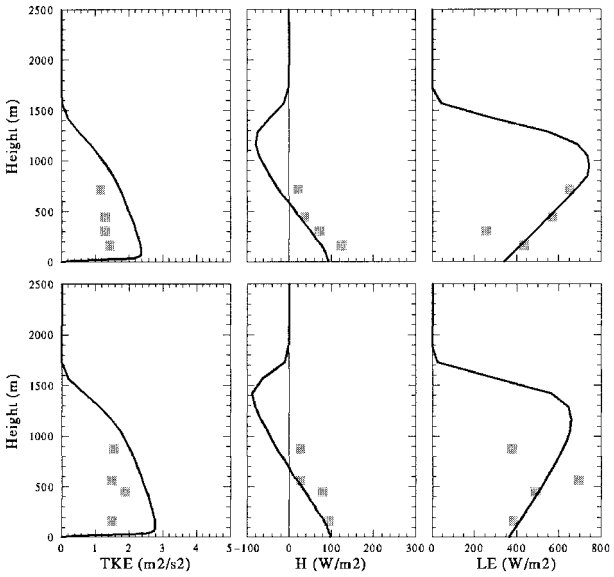

FIG. 14. Same as Fig. 9 but for the simulation using the BL turbulent length scales, for 28 Jun 1996.

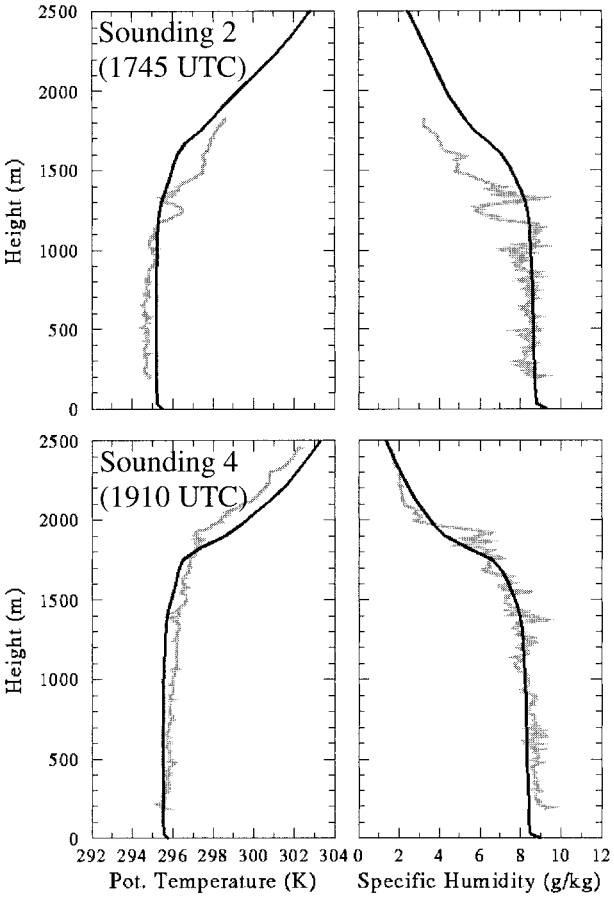

FIG. 15. Same as Fig. 8 but for the simulation using the BL turbulent length scales, for 15 Jun 1996.

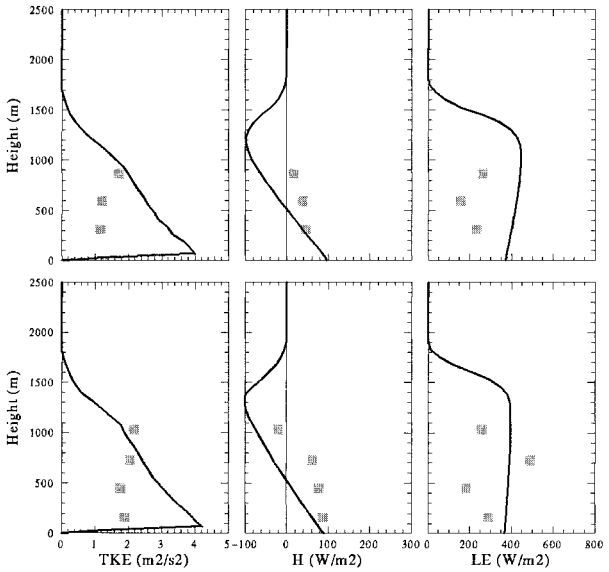

FIG. 16. Same as Fig. 9 but for the simulation using the BL turbulent scales, for 15 Jun 1996. The two observational periods are centered at 1730 UTC (top) and at 1820 UTC (bottom).

quite similar to that observed (see Fig. 15). The simulated deepening rate of the PBL occurs too early since the inversion is already quite high (~1600 m) at 1745 UTC, when observations show a shallower mixed layer (~1200 m) at this time. Thus, the PBL's deepening rate between 1745 and 1910 UTC is still greatly underestimated by the model, and therefore we cannot infer from these results that the inclusion of BL calculations improves the simulated evolution of the PBL during 15 June (cf. Figs. 10 and 15). This conclusion is reinforced when comparing observed versus simulated TKE and turbulent sensible heat fluxes (see Fig. 16). Even more so than for the other case, the low-level TKE is overpredicted by the model while the sensible heat fluxes are underpredicted, showing again that entrainment processes at the top of the boundary layer may be overactive with this formulation (this overactivity is also suggested by the large negative heat fluxes near z_i). The study of Cuxart et al. (1994) also indicated that the BL formulation produced more active entrainment at the top of the mixed layer.

The above results are a bit disappointing, especially when considering that Cuxart et al. (1994) showed that a TKE-based boundary layer scheme similar to the one used in the present study (including the BL formulation for the turbulent mixing lengths) could be as skillful for reproducing the evolution of a convective PBL as a more complex scheme based on turbulent transilient theory could be. We must point out, however, that, even though the choice of averaging for l_{up} and l_{down} relies on the physical considerations described above, this choice remains arbitrary, and it is conceded that other types of averaging could be more appropriate for the simulation of the PBLs observed on 15 and 28 June.

To examine the sensitivity of the PBL simulations to the averaging strategy, another test was done using harmonic averaging for the turbulent mixing length while keeping the same geometric averaging as before for λ_ϵ (see expt BL2 in Table 4). The results indicate that the simulated evolution of the PBL is sensitive to the averaging technique employed, as shown by the θ and q_v profiles for the last sounding performed on 15 June (Fig. 17). When using the harmonic average for λ, the PBL essentially is divided into two layers: a well-mixed layer

TABLE 4. Turbulent lengths for the BL numerical experiments.

Experiment name	Mixing length	Dissipation length
BL	$\lambda = \min(l_{up}, l_{down})$	$\lambda_\epsilon = (l_{up} l_{down})^{1/2}$
BL2	$\frac{1}{\lambda} = \frac{1}{2}\left(\frac{1}{l_{up}} + \frac{1}{l_{down}}\right)$	$\lambda_\epsilon = (l_{up} l_{down})^{1/2}$
BL3	$\lambda = \min(l_{up}, l_{down})$	$\lambda_\epsilon = \left(\frac{1 - \mathrm{Ri}_{flux}}{1 - 2\mathrm{Ri}_{flux}}\right)\lambda$
BL4	$\frac{1}{\lambda} = \frac{1}{2}\left(\frac{1}{l_{up}} + \frac{1}{l_{down}}\right)$	$\lambda_\epsilon = \left(\frac{1 - \mathrm{Ri}_{flux}}{1 - 2\mathrm{Ri}_{flux}}\right)\lambda$

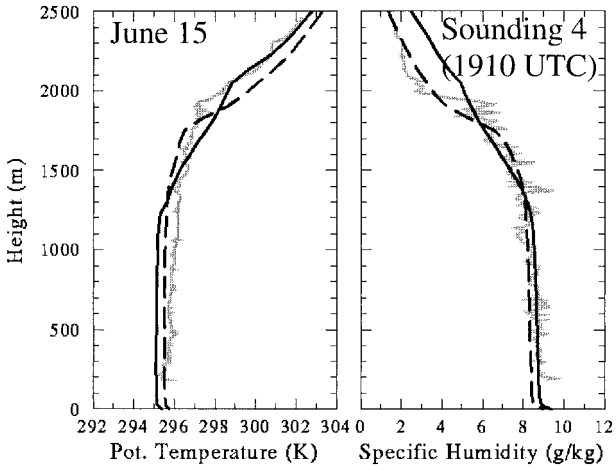

FIG. 17. Comparison of simulated potential temperature (K) and specific humidity (g kg^{-1}) profiles using different strategies for the averaging of l_{up} and l_{down} with observations (gray) from the last sounding performed on 15 Jun. The dashed lines are for the original BL simulation and the full lines are for simulation BL2 (see Table 4).

at low levels, capped by a mere stable (entrainment) layer. Even though certain aspects of this modification may seem to be an improvement over the one obtained using Eq. (10) (except for q_v above the PBL, which is too large by about 2 g kg^{-1}), it is difficult to judge which formulation is superior, and such a sensitivity to this more or less arbitrary aspect of the turbulence scheme clearly is undesirable. Therefore, efforts to improve the performance and make the BL technique less arbitrary are now discussed.

c. *Linking the λ and λ_ϵ turbulent lengths in the BL technique*

One distinct feature of the current turbulence scheme is that two turbulent length scales (i.e., λ and λ_ϵ) have to be specified in order to predict the evolution of the vertical diffusion coefficients and the TKE [see Eqs. (4) and (5)]. When using the BL technique, this translates into twice averaging l_{up} and l_{down} in an ad hoc manner, which is undesirable because the evolution of the simulated PBL is sensitive to the averaging process (see Fig. 17).

The problem of the specification of turbulent length scales has been known for quite some time and other techniques (still based on TKE) have been examined (see Holt and Raman 1988). The E–ϵ technique is perhaps the most popular of these techniques (Detering and Etling 1985; Duynkerke and Driedonks 1987; Holt and Raman 1988); it includes prognostic equations for both TKE and its dissipation rate ϵ, so that the vertical diffusion coefficients can be expressed as a function of these two quantities without involving any turbulent length scales. It must be realized, however, that the prognostic calculations for ϵ in this technique are analogous to prognostic calculations for λ when taking it equal to λ_ϵ (see Detering and Etling 1985; Holt and Raman 1988). Thus, the BL formulation has the advantage (in addition to involving nonlocal calculations) of allowing different values for the two turbulent lengths. What is crucial, then, is to represent correctly these two length scales.

Obviously, it would be helpful if a mathematical relationship could be established between λ and λ_ϵ; then l_{up} and l_{down} would be averaged only once (for either λ or λ_ϵ). Assuming quasi stationarity and neglecting vertical diffusion in the heat flux equation, Therry and Lacarrère (1983) showed that Eq. (4) for the vertical diffusion coefficients implies that the turbulent lengths λ and λ_ϵ must differ and be related by

$$\lambda = C'(\overline{w'^2}/E)\lambda_\epsilon, \tag{11}$$

where C' is a numerical constant. Using a simplified rate equation for $\overline{w'^2}$ to represent explicitly $\overline{w'^2}/E$, they further showed that

$$\lambda = \left[1 + \frac{g}{\theta_v}\frac{(\overline{w'\theta_v'})\lambda_\epsilon}{cE^{3/2}}\right]\lambda_\epsilon, \tag{12}$$

where c is the same constant as in Eq. (5). The above two equations indicate not only that the two turbulent lengths are not equal, but also that λ is greater than λ_ϵ in convectively unstable conditions (i.e., when $\overline{w'\theta_v'} > 0$). This relationship differs from what is done in both the local (in which $\lambda = \lambda_\epsilon$) and BL techniques (in which $\lambda < \lambda_\epsilon$ near the upper and lower edges of the PBL). Obviously, this different relationship between the two turbulent lengths can have a nonnegligible impact on the predicted turbulence and the PBL's evolution, as will be shown below.

It is possible, as shown in appendix B, to simplify further the above relationship by assuming quasi stationarity and by neglecting the transport term in the TKE equation [i.e., Eq. (5)]. We then obtain

$$\lambda = \left(\frac{1 - 2\mathrm{Ri}_{\mathrm{flux}}}{1 - \mathrm{Ri}_{\mathrm{flux}}}\right)\lambda_\epsilon, \tag{13}$$

where $\mathrm{Ri}_{\mathrm{flux}}$ is the ''flux'' Richardson number:

$$\mathrm{Ri}_{\mathrm{flux}} = \frac{\left(\frac{g}{\theta_v}\right)\overline{w'\theta_v'}}{\overline{w'u'}\frac{\partial U}{\partial z} + \overline{w'v'}\frac{\partial V}{\partial z}}. \tag{14}$$

For the next simulations, named BL3 in Table 4, the turbulent mixing length λ is still given by $\min(l_{up}, l_{down})$, but λ_ϵ is now obtained using Eq. (13).

With this strategy, the PBL simulation for both cases is clearly improved relative to the local and original BL formulations. For the 28 June case, both the simulated soundings and turbulent fluxes agree with observations at least as well as those from the local formulation (cf. Figs. 8, 9 and 18, 19), indicating that specifying the

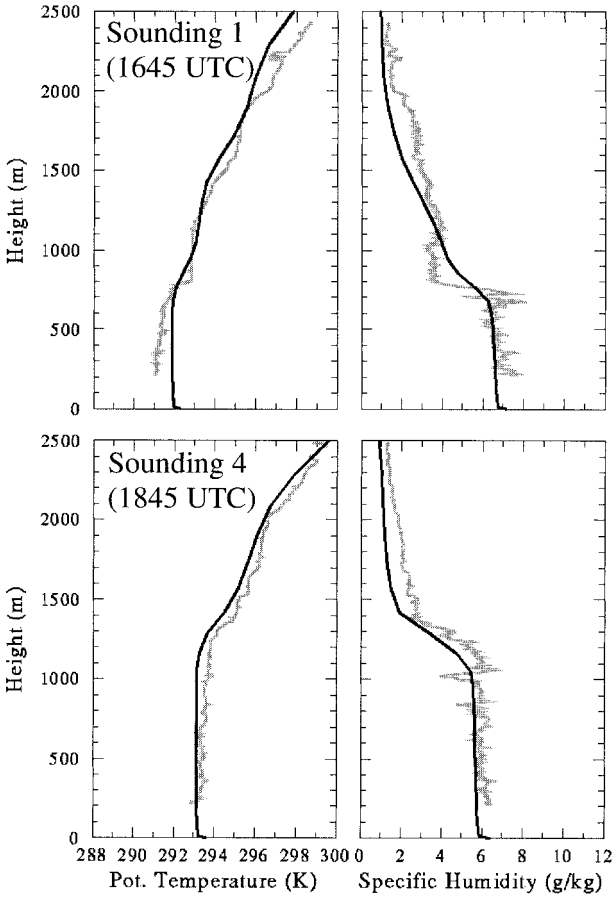

FIG. 18. Same as Fig. 8 but for the simulation using the BL turbulent scales with Eq. (13) as a relationship between the two mixing lengths λ and λ_ϵ, for 28 Jun 1996.

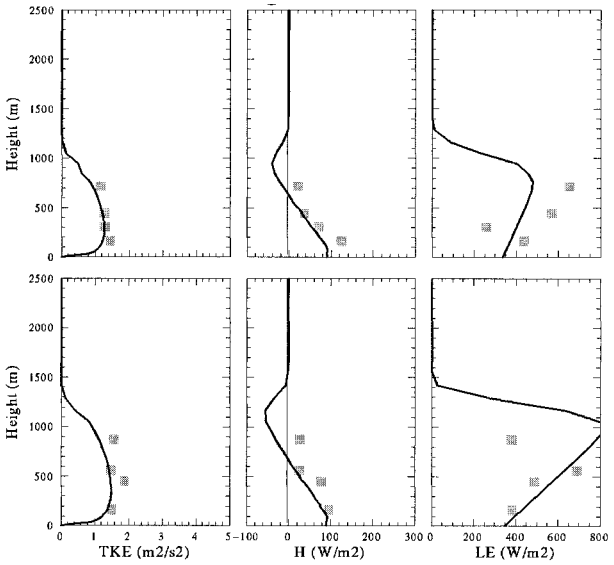

FIG. 19. Same as Fig. 9 but for the simulation using the BL turbulent length scales with Eq. (13) as a relationship between the two mixing lengths λ and λ_ϵ, for 28 Jun 1996.

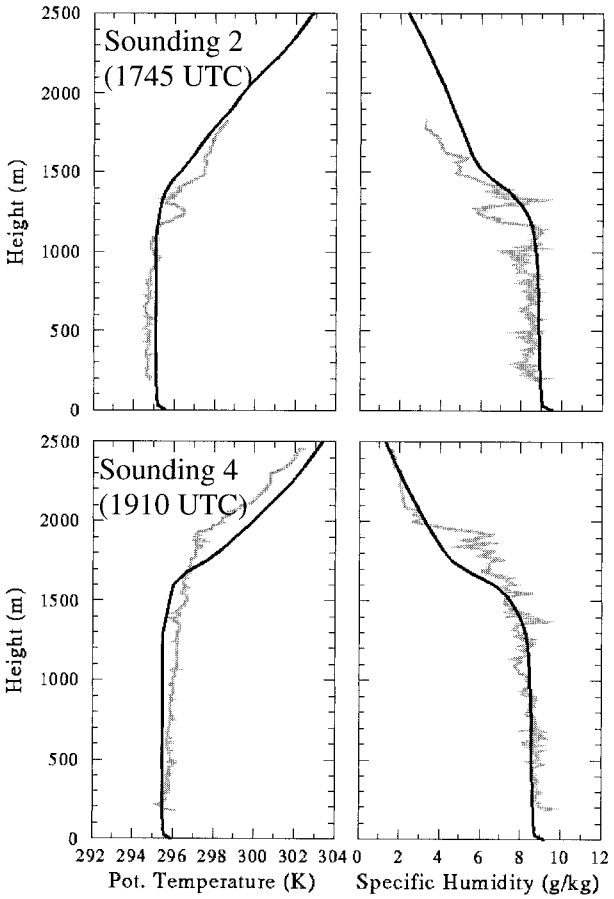

FIG. 20. Same as Fig. 8 but for the simulation using the BL turbulent length scales with Eq. (13) as a relationship between the two mixing lengths λ and λ_ϵ, for 15 Jun 1996.

relationship between λ and λ_ϵ is beneficial to the BL technique for this case (see Figs. 13 and 14). In particular, the evolution of the well-mixed layer fits better the observations, as it is slower than in the original BL technique. Also, the shape of the TKE profile is almost constant with height, as observed. The turbulent fluxes of sensible and latent heat are of the right magnitude (except for LE at 1720 UTC) with more realistic entrainment at the top of the well-mixed layer.

For the 15 June PBL, the simulated θ and q_v profiles agree better with observations, the timing being better than that for both the local formulation, with a slightly faster deepening rate for the mixed layer between 1745 and 1910 UTC (cf. Figs. 10 and 20), and the original BL formulation, which developed earlier a very thick mixed layer at 1745 UTC (cf. Figs. 15 and 20). More impressive is the improvement in the simulated TKE and turbulent fluxes necessary to generate this PBL's evolution (cf. Figs. 11, 16, and 21): the TKE, while still overestimated, is more constant with height and smaller (especially at low levels) than that seen with both the local and the original BL formulations, and the turbulent sensible heat fluxes are now of the right magnitude

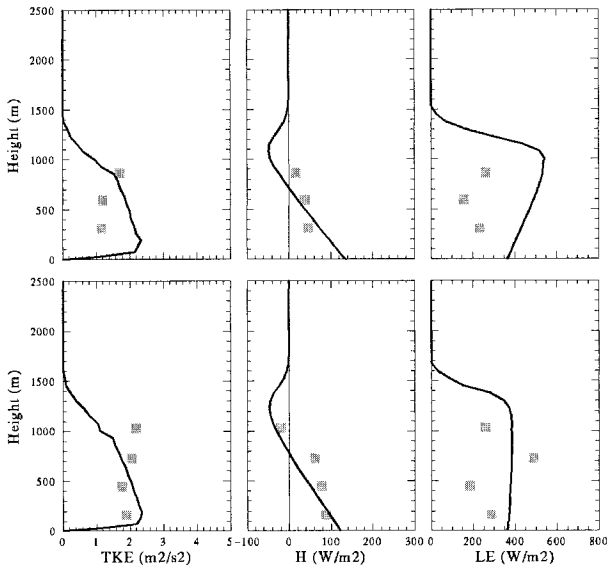

FIG. 21. Same as Fig. 9 but for the simulation using the BL turbulent scales with Eq. (13) as a relationship between the two mixing lengths λ and λ_ϵ, for 15 Jun 1996. The two observational periods are centered at 1730 UTC (top) and at 1820 UTC (bottom).

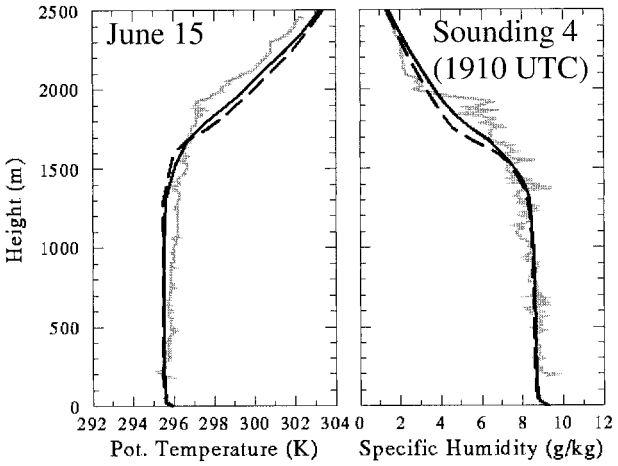

FIG. 22. Same as Fig. 17 but for the simulations using the BL turbulent scales with Eq. (13) as a relationship between the two mixing lengths λ and λ_ϵ. The dashed lines are for the BL3 simulation and the full lines are for simulation BL4 (see Table 4).

(somewhere between the smaller and larger fluxes from the original BL and local formulations, respectively) with moderate entrainment. Only the latent heat fluxes still show large discrepancies with the observations.

It is worthwhile, at this point, to explain further the nature of the improvement that results from the use of Eq. (13) in the context of this study's experimental design. When only comparing the θ and q_v profiles between the local and modified BL formulations, the improvement related to the use of the BL mixing lengths together with Eq. (13) may not seem important. But it must be understood that the slightly better evolution of these profiles obtained with the new formulation occurs with surface fluxes of sensible heat that are about 30% smaller than those in the local simulation. These new fluxes, which are in better agreement with observations, are directly influenced by the soil water contents, which were calibrated so as to minimize the errors in surface air temperature and humidity content. When the soil water contents obtained by calibration with the new PBL formulation are used also to redo the local simulation of the 15 June case, the resulting PBL is even shallower than the poor results shown in Figs. 10 and 11, leading to a worse comparison against observations even though the surface fluxes are more realistic.

Although its amplitude may be somewhat surprising, the change resulting from specifying the relationship between the two turbulent lengths may be explained simply. With the modification to the BL technique, λ_ϵ is forced to be smaller than λ everywhere in the convective PBL except in the entrainment zone where the kinematic heat fluxes $\overline{w'\theta'}$ are less than 0 [see Eq. (12)]. TKE is thus more dissipated in the bulk of the PBL in comparison with both the original BL and local formulations [see Eq. (5)] and has smaller values in the lowest levels (cf. Figs. 9–11, 14–16, and 19–21). Entrainment also is reduced in comparison with the original BL technique [more dissipation because λ_ϵ from Eq. (13) is smaller than that derived from Eq. (10), even though $\lambda_\epsilon > \lambda$ with both formulations] but still remains larger than for the local formulation. As a final result, the reduced turbulence and intermediate entrainment (as compared to the local and original BL formulations) lead to simulations of the PBL that compare better with observations.

Finally, when using Eq. (13) to relate the two turbulent lengths, the sensitivity of the results to the averaging method for λ is greatly reduced, as shown in Fig. 22 for experiment BL4 in Table 4. There are some differences when using the harmonic l_{up}–l_{down} averaging instead of the original formulation of Bougeault and Lacarrère (1989), but these are minor compared to those obtained for the same sensitivity experiment using the original method of averaging the l_{up} and l_{down} scales (cf. Figs. 17 and 22). This reduced sensitivity is another advantage of relating the two turbulent length scales in a more physical way through Eq. (13).

6. Summary and conclusions

The main purpose in this study is to evaluate the performance of a TKE-based turbulence scheme in reproducing the rapid boundary layer evolution observed for two MERMOZ cases that occurred in quite different environmental conditions. In this context, the impact of including nonlocal features in the boundary layer scheme is examined.

Using the original formulation of the turbulence scheme (in which the vertical diffusion coefficients are determined locally), the model is able to reproduce quite

well the evolution of the vertical structures and turbulent fluxes (including TKE) observed in the boundary layer for a strongly convective case (i.e., 28 June), labeled as the best clear day of the experiment because of considerable large-scale subsidence and weak vertical wind shear. For an intermediate convective case with moderate convection and shear-driven processes (i.e., 15 June), the more rapid PBL evolution (the capping effect of large-scale subsidence is weaker and the destabilizing effect of vertical wind shear is larger for this case) is underestimated by the model, even though the TKE and sensible heat fluxes are considerably overpredicted. It thus seems, in agreement with other studies, that the *local* formulation of the K coefficients is not always adequate for strongly convective PBLs, in which the mixing caused by the larger eddies is felt in a *nonlocal* manner throughout the depth of the PBL.

For this reason, other formulations of the turbulence scheme that allow such nonlocal mixing are tested for the same two cases. It is found first that the inclusion of nonlocal (or countergradient) terms in the vertical diffusion equation [Eq. (2)] has a negligible impact on the simulated PBLs, probably because the PBL depths are relatively large and the sensible heat fluxes are relatively small for these two MERMOZ cases.

The PBL's evolution is found to be more sensitive to the specific formulation of the turbulent length scales used in the TKE scheme. Using the strategy described in Bougeault and Lacarrère (1989) results in the well-mixed layer for both cases being much deeper than that derived from the local simulations, even though the turbulent sensible heat fluxes are smaller. The entrainment processes at the top of the well-mixed layer are enhanced with the new turbulent length scales, so that weaker sensible heat fluxes can generate a rapid evolution of the PBL. Similarly, the TKE is larger when using this formulation, especially at low levels. Unfortunately, the verification against observations is not improved by including these nonlocal mixing length calculations. Indeed, some deterioration is found for the strongly convective case of 28 June.

It is further noted that the results are sensitive to the particular averaging method used to obtain λ and λ_ϵ. Based on the work of Therry and Lacarrère (1983), a relationship between the two turbulent scales is proposed [Eq. (13)] that, in addition to reducing some arbitrariness in the BL scheme and to providing a more physical basis, helps to improve the PBL simulation for both cases. Moreover, the results are less sensitive to the averaging of l_{up} and l_{down} when using this λ–λ_ϵ relationship.

In summary, significant differences among the various formulations tested are noted during the period of rapid PBL growth. Discrepancies with observations are found with all formulations, and it is not easy to identify the clear superiority of one particular formulation. However, a more physical relationship between the two turbulent scales, based on Eq. (13), leads to a more active entrainment zone than does the local formulation, and exhibits a more realistic level of activity than the original formulation of BL does [Eq. (10)]. These two results lead to a better overall agreement with observations of the mixed layer evolution, the turbulent structures, and the fluxes (except, perhaps, for the latent heat fluxes at specific times) and to a significant reduction in the sensitivity to the formulations used for the length scales. It should be stressed that the comparison with observations presented in this study can give only a first indication of the quality of the new parameterization, and that many more simulations, involving different types of meteorological situations, should be performed in order to claim the superiority of one formulation over another.

The reasons why the model is not able to reproduce in a more realistic manner the deepening of 15 June's well-mixed layer, even with the use of the nonlocal turbulent lengths, may be related to the environmental conditions in which the layer developed or to other shortcomings of the turbulence scheme (related to PBL-top entrainment, e.g.). Although the vertically varying cooling caused by horizontal advection is represented well by the three-dimensional model, the relatively coarse vertical resolution in the entrainment region may not be sufficient to simulate correctly the entrainment and could be partly responsible for the discrepancy between the observed and simulated PBLs. Another possibility is that the boundary layer clouds that formed in the proximity of the sounding site near the end of the observing period might have indirectly influenced (by advective processes, for example) the evolution of the upper part of the PBL by promoting entrainment in the region of interest.

These topics related to entrainment processes occurring near the top of the boundary layer were the main subjects of interest for a follow-up experiment to MERMOZ that was conducted in the same area during August 1997. In this field program, emphasis was placed on measurements in the upper portion of the boundary layer for both clear and cloudy cases. Also, the rapid evolution of the boundary layer in the morning hours has been well documented in this experiment. Verification of model results against these new observations is under way to improve the representation of entrainment.

Acknowledgments. We would first like to thank all those who participated in the preparation and field phases of the MERMOZ experiment. During the course of this work, we particularly appreciated the help from J. He, V. Lee, and B. Bilodeau (RPN/AES), M. Wasey (ARMP/AES), and M. Bastian (NRC). N. Donaldson (ARMP/AES) provided Fig. 5. This work also benefited from discussions with Y. Delage and C. Girard (RPN/AES). Finally, the lead author was supported by a scholarship from the National Science and Engineering Research Council of Canada.

APPENDIX A

The Sequential Assimilation Technique

The basic idea of the technique proposed by Mahfouf (1991) is to relate errors in soil moisture contents (w_g and w_2 for the superficial and deep soil layers) to errors in low-level air temperature (T) and relative humidity (RH), following the linear equations

$$\delta w_g = w_g^a - w_g^f = \alpha_1(T^o - T^f) + \alpha_2(\mathrm{RH}^o - \mathrm{RH}^f), \quad \text{and} \quad \text{(A1)}$$

$$\delta w_2 = w_2^a - w_2^f = \beta_1(T^o - T^f) + \beta_2(\mathrm{RH}^o - \mathrm{RH}^f), \quad \text{(A2)}$$

where the superscripts *a*, *f*, and *o* refers to ''analyzed,'' ''forecast,'' and ''observed,'' respectively.

The problem therefore consists in evaluating the α_1, α_2, β_1, and β_2 coefficients for all types of soils, vegetation, and meteorological conditions. Based on the work of Mahfouf (1991), who estimated the statistical distribution of these coefficients at each local solar time using a Monte Carlo method, Bouttier et al. (1993) proposed an analytical formulation of the coefficients (continuous functions of the surface characteristics), which later was modified by Giard and Bazile (1999) to yield

$$\alpha_1 = f(\mathrm{txt})(1 - \mathrm{veg})[a_0^T(t) + a_1^T(t)\mathrm{veg} + a_2^T\mathrm{veg}^2], \quad \text{(A3)}$$

$$\alpha_2 = f(\mathrm{txt})(1 - \mathrm{veg})[a_0^H(t) + a_1^H(t)\mathrm{veg} + a_2^H\mathrm{veg}^2], \quad \text{(A4)}$$

$$\beta_1 = f(\mathrm{txt})\left\{(1 - \mathrm{veg})[b_0^T(t) + b_1^T(t)\mathrm{veg} + b_2^T(t)\mathrm{veg}^2] + \mathrm{veg}[c_0^T(t) + c_1^T(t)\mathrm{veg}]\frac{\mathrm{LAI}}{R_{s\,\min}}\right\}, \quad \text{(A5)}$$

$$\beta_2 = f(\mathrm{txt})\left\{(1 - \mathrm{veg})[b_0^H(t) + b_1^H(t)\mathrm{veg} + b_2^H(t)\mathrm{veg}^2] + \mathrm{veg}[c_0^H(t) + c_1^H(t)\mathrm{veg}]\frac{\mathrm{LAI}}{R_{s\,\min}}\right\}, \quad \text{(A6)}$$

$$f(\mathrm{txt}) = \frac{\delta w(\mathrm{txt})}{\delta w(\mathrm{loam})}, \quad \text{and} \quad \delta w = w_{\mathrm{fc}} - w_{\mathrm{wilt}}, \quad \text{(A7)}$$

where txt is the soil texture (e.g., sand, clay), veg is the fraction of vegetation covering a model grid area, LAI is the leaf area index (area of leaf coverage per surface area unit), $R_{s\,\min}$ is the minimum stomatal resistance, and w_{fc} and w_{wilt} are the volumetric water contents at the field capacity and wilting point, respectively. Note that $f(\mathrm{txt})$ equals 1.0 in this study since loam is chosen as the soil type for the entire integration domain. Finally, the time-dependent coefficients a_i^T, a_i^H, b_i^T, and b_i^H were calculated to fit the continuous functions to a large sample of α and β coefficients computed exactly using the Monte Carlo method [see Bouttier et al. (1993) for more details].

For the temperature, the surface increments are related directly to model errors at the anemometer level (i.e., 2 m), following

$$\delta T_S = T_S^a - T_S^f = T_{2m}^o - T_{2m}^f$$

$$\delta T_2 = T_2^a - T_2^f = \frac{(T_{2m}^o - T_{2m}^f)}{\tau}, \quad \text{(A8)}$$

where $\tau = 2\pi$ for ISBA.

APPENDIX B

Relationship between λ and λ_ϵ

For quasi-stationary turbulent flow with negligible vertical transport of turbulence, the TKE prognostic equation can be written as

$$\underbrace{\frac{cE^{3/2}}{\lambda_\epsilon}}_{\mathrm{D}} = \underbrace{-\overline{w'u'}\frac{\partial U}{\partial z} - \overline{w'v'}\frac{\partial V}{\partial z}}_{\mathrm{M}} + \underbrace{\frac{g}{\theta_v}\overline{w'\theta_v'}}_{\mathrm{B}}, \quad \text{(B1)}$$

where M and B are the mechanical and buoyancy terms. Using this terminology, Eqs. (12) and (14) can be expressed as

$$\lambda = (1 + \mathrm{B/D})\lambda_\epsilon$$

$$\mathrm{Ri}_{\mathrm{flux}} = -\mathrm{B/M}. \quad \text{(B2)}$$

Substituting D = M + B, we then obtain

$$\lambda = \left(\frac{1 + 2\mathrm{B/M}}{1 + \mathrm{B/M}}\right)\lambda_\epsilon$$

$$\lambda = \left(\frac{1 - 2\mathrm{Ri}_{\mathrm{flux}}}{1 - \mathrm{Ri}_{\mathrm{flux}}}\right)\lambda_\epsilon. \quad \text{(B3)}$$

REFERENCES

Abdella, K., and N. McFarlane, 1997: A new second-order turbulence closure scheme for the planetary boundary layer. *J. Atmos. Sci.*, **54,** 1850–1867.

Alapaty, K., J. E. Pleim, S. Raman, D. S. Niyogi, and D. W. Byun, 1997: Simulation of atmospheric boundary layer processes using local- and nonlocal-closure schemes. *J. Appl. Meteor.*, **36,** 214–233.

André, J.-C., G. De Moor, P. Lacarrère, G. Therry, and R. du Vachat, 1978: Modeling the 24-hour evolution of the mean and turbulent structures of the planetary boundary layer. *J. Amos. Sci.*, **35,** 1861–1883.

——, J.-P. Goutorbe, and A. Perrier, 1986: HAPEX-MOBILHY: A hydrologic atmospheric experiment for the study of water budget and evaporation flux at the climatic scale. *Bull. Amer. Meteor. Soc.*, **67,** 138–144.

Barnes, S. L., 1964: A technique for maximizing details in numerical weather map analysis. *J. Appl. Meteor.*, **3,** 396–409.

Benoit, R., J. Côté, and J. Mailhot, 1989: Inclusion of a TKE boundary layer parameterization in the Canadian regional finite-element model. *Mon. Wea. Rev.*, **117,** 1726–1750.

——, M. Desgagné, P. Pellerin, S. Pellerin, Y. Chartier, and S. Desjardins, 1997: The Canadian MC2: A semi-Lagrangian, semi-implicit wideband atmospheric model suited for finescale process studies and simulation. *Mon. Wea. Rev.*, **125,** 2382–2415.

Berkowicz, R., 1984: Spectral methods for atmospheric diffusion modeling. *Bound.-Layer Meteor.,* **30,** 201–220.

Bougeault, P., and J.-C. André, 1986: On the stability of the third-order turbulence closure for the modeling of the stratocumulus-topped boundary layer. *J. Atmos. Sci.,* **43,** 1574–1581.

——, and P. Lacarrère, 1989: Parameterization of orography-induced turbulence in a mesobeta-scale model. *Mon. Wea. Rev.,* **117,** 1872–1890.

Bouttier, F., J.-F. Mahfouf, and J. Noilhan, 1993: Sequential assimilation of soil moisture from atmospheric low-level parameters. Part I: Sensitivity and calibration studies. *J. Appl. Meteor.,* **32,** 1335–1351.

Chrobok, G., S. Raasch, and D. Etling, 1992: A comparison of local and nonlocal turbulence closure methods for the case of a cold air outbreak. *Bound.-Layer Meteor.,* **58,** 69–90.

Cuijpers, J. W. M., and A. A. M. Holtslag, 1998: Impact of skewness and nonlocal effects on scalar and buoyancy fluxes in convective boundary layers. *J. Atmos. Sci.,* **55,** 151–162.

Cuxart, J., P. Bougeault, P. Lacarrère, J. Noilhan, and M. R. Soler, 1994: A comparison between transilient turbulence theory and the exchange coefficient model approaches. *Bound.-Layer Meteor.,* **67,** 251–276.

Deardorff, J. W., 1966: The counter-gradient heat flux in the lower atmosphere and in the laboratory. *J. Atmos. Sci.,* **23,** 503–506.

——, 1972: Theoretical expression for the countergradient vertical heat flux. *J. Geophys. Res.,* **77,** 5900–5904.

Delage, Y., 1997: Parameterising sub-grid scale vertical transport in atmospheric models under statically stable conditions. *Bound.-Layer Meteor.,* **82,** 23–48.

——, and C. Girard, 1992: Stability functions correct at the free convection limit and consistent for both the surface and Ekman layers. *Bound.-Layer Meteor.,* **58,** 19–31.

Detering, H. W., and D. Etling, 1985: Application of the E–ϵ turbulence model to the atmospheric boundary layer. *Bound.-Layer Meteor.,* **33,** 113–133.

Duynkerke, P. G., and A. G. M. Driedonks, 1987: A model for the turbulent structure of the stratocumulus-topped atmospheric boundary layer. *J. Atmos. Sci.,* **44,** 43–64.

Ebert, E. E., U. Schumann, and R. B. Stull, 1989: Nonlocal turbulent mixing in the convective boundary layer evaluated from large-eddy simulation. *J. Atmos. Sci.,* **46,** 2178–2207.

Fiedler, B. H., and C.-H. Moeng, 1985: A practical integral closure model for mean vertical transport of a scalar in a convective boundary layer. *J. Atmos. Sci.,* **42,** 359–363.

Fouquart, Y., and B. Bonnel, 1980: Computations of solar heating of the earth's atmosphere: A new parameterization. *Contrib. Atmos. Phys.,* **53,** 35–62.

Garand, L., 1983: Some improvements and complements to the infrared emissivity algorithm including parameterization of the absorption in the continuum region. *J. Atmos. Sci.,* **40,** 230–344.

Garratt, J. R., G. D. Hess, W. L. Physick, and P. Bougeault, 1996: The atmospheric boundary layer—Advances in knowledge and application. *Bound.-Layer Meteor.,* **78,** 9–37.

Giard, D., and E. Bazile, 1999: Implementation of a new assimilation scheme for soil and surface variables in a global NWP model. *Mon. Wea. Rev.,* in press.

Holt, T., and S. Raman, 1988: A review and comparative evaluation of multilevel boundary layer parameterizations for first-order and turbulent kinetic energy closure schemes. *Rev. Geophys.,* **26,** 761–780.

Holtslag, A. A. M., and C.-H. Moeng, 1991: Eddy diffusivity and countergradient transport in the convective atmospheric boundary layer. *J. Atmos. Sci.,* **48,** 1690–1698.

——, and B. A. Boville, 1993: Local versus nonlocal boundary-layer diffusion in a global climate model. *J. Climate,* **6,** 1825–1842.

——, E. Van Meijgaard, and W. C. De Rooy, 1995: A comparison of boundary layer diffusion schemes in unstable conditions over land. *Bound.-Layer Meteor.,* **76,** 69–95.

Jacquemin, B., and J. Noilhan, 1990: Sensitivity study and validation of a land surface parameterization using the HAPEX-MOBILHY data set. *Bound.-Layer Meteor.,* **52,** 93–134.

Kuo, H. L., 1974: Further studies of the parameterization of the influence of cumulus convection on large-scale flow. *J. Atmos. Sci.,* **31,** 1232–1240.

Lenschow, D. H., and B. B. Stankov, 1986: Length scales in the convective boundary layer. *J. Atmos. Sci.,* **43,** 1198–1209.

Lüpkes, C., and K. H. Schlünzen, 1996: Modelling the arctic convective boundary-layer with different turbulence parameterizations. *Bound.-Layer Meteor.,* **79,** 107–130.

Mahfouf, J.-F., 1991: Analysis of soil moisture from near-surface parameters: A feasibility study. *J. Appl. Meteor.,* **30,** 1534–1547.

——, and B. Jacquemin, 1989: A study of rainfall interception using a land surface parameterization for mesoscale meteorological models. *J. Appl. Meteor.,* **28,** 1282–1302.

Mailhot, J., and R. Benoit, 1982: A finite-element model of the atmospheric boundary layer suitable for use with numerical weather prediction models. *J. Atmos. Sci.,* **39,** 2249–2266.

——, and Coauthors, 1998: The Montreal-96 Experiment on Regional Mixing and Ozone (MERMOZ): An overview and some preliminary results. *Bull. Amer. Meteor. Soc.,* **79,** 433–442.

Mellor, G. L., and T. Yamada, 1974: A hierarchy of turbulence closure models for planetary boundary layers. *J. Atmos. Sci.,* **31,** 1791–1806.

——, and ——, 1982: Development of a turbulence closure model for geophysical fluid problems. *Rev. Geophys. Space Phys.,* **20,** 851–875.

Moeng, C.-H., and D. A. Randall, 1984: Problems in simulating the stratocumulus-topped boundary layer with a third-order closure model. *J. Atmos. Sci.,* **41,** 1588–1600.

——, and P. P. Sullivan, 1994: A comparison of shear- and buoyancy-driven planetary boundary layer flows. *J. Atmos. Sci.,* **51,** 999–1022.

Noilhan, J., and S. Planton, 1989: A simple parameterization of land surface processes for meteorological models. *Mon. Wea. Rev.,* **117,** 536–549.

O'Brien, J. J., 1970: A note on the vertical structure of the eddy exchange coefficient in the planetary boundary layer. *J. Atmos. Sci.,* **27,** 1213–1215.

Pielke, R. A., and Y. Mahrer, 1975: Representation of the heated planetary boundary layer in mesoscale models with coarse vertical resolution. *J. Atmos. Sci.,* **32,** 2288–2308.

Sellers, P. J., F. G. Hall, G. Asrar, D. E. Strebel, and R. E. Murphy, 1988: The First ISLSCP Field Experiment (FIFE). *Bull. Amer. Meteor. Soc.,* **69,** 22–27.

Stull, R., 1984: Transilient turbulence theory. Part I: The concept of eddy-mixing across finite distances. *J. Atmos. Sci.,* **41,** 3351–3367.

——, 1988: *An Introduction to Boundary Layer Meteorology*. Kluwer Academic, 666 pp.

——, 1993: Review of non-local mixing in turbulent atmospheres: Transilient turbulence theory. *Bound.-Layer Meteor.,* **62,** 21–96.

——, and A. G. M. Driedonks, 1987: Applications of the transilient turbulence parameterization to atmospheric boundary-layer simulations. *Bound.-Layer Meteor.,* **40,** 209–239.

Tanguay, M., A. Robert, and R. Laprise, 1990: A semi-implicit semi-Lagrangian fully compressible regional forecast model. *Mon. Wea. Rev.,* **118,** 1970–1980.

Therry, G., and P. Lacarrère, 1983: Improving the eddy kinetic energy model for planetary boundary layer description. *Bound.-Layer Meteor.,* **25,** 63–88.

Troen, I. B., and L. Mahrt, 1986: A simple model of the atmospheric boundary layer; sensitivity to surface evaporation. *Bound.-Layer Meteor.,* **37,** 129–148.

Wyngaard, J. C., and R. A. Brost, 1984: Top-down bottom-up diffusion of a scalar in the convective boundary layer. *J. Atmos. Sci.,* **41,** 102–112.

Zhang, Q., and R. Stull, 1992: Alternative nonlocal descriptions of boundary-layer evolution. *J. Atmos. Sci.,* **49,** 2267–2281.